remote sensing

MDPI

Article

Integrated Reconstruction of Late Quaternary Geomorphology and Sediment Dynamics of Prokljan Lake and Krka River Estuary, Croatia

Ozren Hasan , Natalia Smrkulj * , Slobodan Miko , Dea Brunović, Nikolina Ilijanić and Martina Šparica Miko

Department for Mineral Resources, Croatian Geological Survey, Sachsova 2, 10000 Zagreb, Croatia
* Correspondence: nsmrkulj@hgi-cgs.hr; Tel.: +385-1-616-0798

Abstract: The upper part of the Krka River estuary and Prokljan Lake are a specific example of a well-stratified estuarine environment in a submerged river canyon. Here, we reconstructed the geomorphological evolution of the area and classified the data gathered in the study, integrating multibeam echosounder data, backscatter echosounder data, side-scan sonar morpho-bathymetric surveys, and acoustic sub-bottom profiling, with the addition of ground-truthing and sediment analyses. This led to the successful classification of the bottom sediments using the object-based image analysis method. Additional inputs to the multibeam echosounder data improved the segmentation of the seafloor classification, geology, and morphology of the surveyed area. This study uncovered and precisely defined distinct geomorphological features, specifically submerged tufa barriers and carbonate mounds active during the Holocene warm periods, analogous to recent tufa barriers that still exist and grow in the upstream part of the Krka River. Fine-grained sediments, classified as estuarine sediments, hold more organic carbon than coarse-grained sediments sampled on barriers. A good correlation of organic carbon with silt sediments allowed the construction of a prediction map for marine sedimentary carbon in this estuarine/lake environment using multibeam echosounder data. Our findings highlight the importance of additional inputs to multibeam echosounder data to achieve the most accurate results.

Keywords: seabed mapping; seabed classification; multibeam bathymetry; backscatter; tufa; seabed geomorphology; organic carbon in sediment; prediction map

check for updates

Citation: Hasan, O.; Smrkulj, N.; Miko, S.; Brunović, D.; Ilijanić, N.; Šparica Miko, M. Integrated Reconstruction of Late Quaternary Geomorphology and Sediment Dynamics of Prokljan Lake and Krka River Estuary, Croatia. *Remote Sens.* **2023**, *15*, 2588. https://doi.org/10.3390/rs15102588

Academic Editor: Martin Gade

Received: 16 February 2023
Revised: 4 May 2023
Accepted: 11 May 2023
Published: 16 May 2023

1. Introduction

The use of remote sensing acoustic technologies in marine surveys has great potential for the accurate mapping and geomorphological and geological classification of the seabed [1–3]. While some previous studies have used only multibeam echosounder (MBES) data to interpret seabed properties [4,5], others have shown that the use of MBES backscattering (BSE) in addition to MBES bathymetry and its derivatives improves the prediction accuracy of bottom mapping [6,7]. Correct maps of the seabed can be achieved by ground-truthing in the form of direct seabed video observations, sediment sampling, and sediment sample analyses [1,3,8,9]. High-resolution sub-bottom profiles are used as an additional tool for the better interpretation of mapped units and allow insight into the third dimension of the gathered data [10–15].

The highly stratified estuary of the Krka River is characterized by a low terrigenous input due to its mostly karstic watershed and numerous travertine barriers, lakes, and waterfalls upstream of the estuary [16,17]. Most studies of the study area have focused on the biological, hydrological, hydrodynamic, and geochemical characteristics of the water column or bottom surface. Phytoplankton and bacterial diversity [17,18], abundance [19–22], and dynamics [23,24] have been intensively studied, as well as the physical and chemical properties of the river water column [25–29] and its sediments [30]. The estuary of the Krka

River ends upstream at the large Skradinski Buk tufa barrier/waterfall. The upstream part is a national park with well-studied tufa barriers, surficial lake sediments, and a water column, as well as the whole land surface area. The mineralogy, geochemistry, diagenesis, and formation of barriers have been studied [31–33], as well as hydrology [34,35]. Recent tufa barriers are numerous in the upstream part of the Krka River. These unique karst geomorphological features, which grow as algae and mosses, are encrusted by carbonate and are controlled by the outgassing of CO_2 or its consumption by plants [31,36].

During the Last Glacial Maximum (LGM), when the sea level was up to 130 m lower than today [37–39], karst rivers along the eastern Adriatic coast were formed and incised their valleys into the land [40]. Consequently, the Krka River may have formed a wide delta between the island of Žirje in the northwest and the mainland in the southeast. During the rapid Holocene relative sea-level rise, the sea flooded hypsometrically lower parts of the rivers along the eastern Adriatic coast, and salt-wedge estuaries such as the Krka or Zrmanja Rivers [28,41,42] were formed. Besides the relative sea-level rise, other factors may control hydrodynamic and geomorphic processes, such as inherited topography, the morphology of the estuary, or the paleoclimate [43,44]. The barriers in the Krka River prevented direct marine flooding during the mid-Holocene. There are not enough data available about the evolutionary history of Quaternary deposits along the eastern Adriatic coast, which means that the Quaternary sea-level changes in this area are still not well-defined. The oldest ages of the still-active tufa barrier system of the Krka River at Skradinski Buk were determined to be 8000 y BP [31]. Upstream from Skradinski Buk, outcrops of a collapsed tufa barrier tower up to 20 m above the tufa barrier of Skradinski Buk (the top of the barrier is at +46 m above sea level (a.s.l.)), which were dated to MIS 5e [31]. Tufa barrier growth enabled the formation of waterfalls and a system of small lakes. Tufa barriers are "constructive waterfalls", a propagating type of headwall that constantly accumulates and progrades [45]. As the barriers continuously grow as long as they are exposed to air, it causes the deepening of plunge pool scours until the sea level causes a cessation of tufa growth. The mechanism of formation is well-explained, where plunge pools initially filled with sediment are scoured [46–49]. The depth of the plunge pool scours depends on water discharge, waterfall drop height, and the particle size of sedimented and suspended material [46,50,51]. The rate of plunge pool scour decreases as the pool deepens, the flow velocity lowers, or an increase in sediment supply forces them to aggrade [46,50]. Accordingly, a greater waterfall height and finer grain size create deeper pool depths until equilibrium is reached. Those plunge pools can be detectable in the sub-bottom profiles.

The shelf sediments present significant carbon storage in surficial sediments, but there are large uncertainties within the estimate [52]. Terrestrial carbon stores have been reasonably well-mapped and have established protocols, but only a small portion of the seabed has been mapped and is therefore less understood [9]. At present, the European Commissions' European Marine Observation and Data network (EMODnet) Geology project is a main European driver for the creation of seabed substrate and habitat maps, but there is no specific research dedicated to sediment carbon storage. An attempt to standardize organic carbon distribution in sediments, based on MBES backscatter data and sediment grain size, has been proposed by [9]. Several other studies have shown that the distribution of organic matter in surface sediments is directly related to the particle size distribution and mineral composition of those sediments [53–56].

This study investigated the upper part of the 24 km-long Krka River estuary situated on the eastern Adriatic coast, which comprises the submerged Krka River canyon and Prokljan Lake system that existed before the Holocene relative sea-level rise. To date, the morphology of Prokljan Lake and the upper region of the Krka River estuary has only been mapped at a coarse resolution that did not detect distinct morphological features present in the investigated area. This paper aimed to use high-resolution geophysical methods in conjunction with surficial estuarine sediment data analyses to define and map the estuary seabed geology and geomorphology, as well as the distribution of sediment properties. Based on the high-resolution MBES bathymetry, BSE data, sub-bottom profiler

(SBP) data, and side-scan sonar (SSS) survey, combined with ground-truthing (sediment grabs and video transects) and various analyses of the collected sediments, such as grain size, magnetic susceptibility, mineralogical composition, and organic carbon, we mapped the estuarine seabed with the use of object-based image analysis (OBIA). OBIA has been used in relatively recent sea bottom mapping surveys [12,57–60]. The method gives raster data a new dimension, recognizing and taking into account pixel values and allowing the correlation of BSE variability to seabed sediment properties [61]. This enables the creation of high-resolution sediment-type maps. The newly obtained data and modeled maps can be applied to marine benthic habitat mapping, while the high-resolution bathymetry can be used to better understand and model the stratified estuary of the Krka River.

2. Regional Settings

The Krka River estuary is situated on the eastern Adriatic coast near the city of Šibenik (Figure 1). The study area is located in a karst region and developed within the External Dinarides, which are part of the Adriatic carbonate platform. The platform existed from the late Paleozoic to the Eocene [62]. The platform began to disintegrate in the Late Cretaceous, resulting in the regional emergence of the entire platform, which extended into the Paleogene. The final uplift of the Dinarides occurred during the Oligocene and Miocene. Therefore, the drainage area of the Krka River is composed of Jurassic, Upper Cretaceous, and Eocene limestones [63]. As a result of intense late Pleistocene glaciation, the Krka River canyon has been incised in the karst plateau [63].

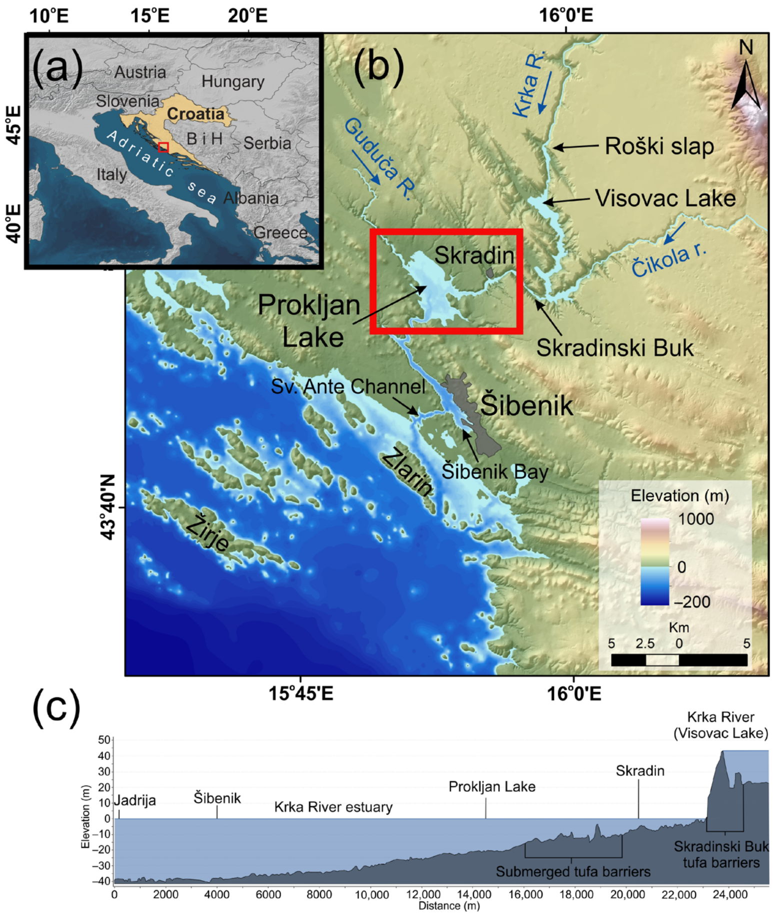

Figure 1. (**a**) Location of the study site in Europe: (**b**) Overview of the area of interest with the study site of Prokljan Lake and Krka River outlined with a red square; (**c**) Profile showing the bottom morphology of the Krka River estuary from Sveti Ante Channel to Skradinski Buk.

The Krka River springs are located at the foot of Dinara Mountain near the town of Knin, and the river discharges into the Adriatic Sea. The hydrographic catchment of this typical groundwater-fed karstic river covers more than 2400 km^2, with a length of 49 km for the freshwater part and an additional 24 km for the estuary [35]. The river flow rates vary significantly, ranging from 0.2 to 5 m^3/s up to 565 m^3/s, with an average annual flow between 40 and 60 m^3/s [35,64]. Numerous tufa barriers and waterfalls occur along the river canyon course. The river ends with the 46 m-high tufa barriers at Skradinski Buk. The tufa barriers and waterfalls, together with a part of the estuary from the foot of the Skradinski Buk barrier and the town of Skradin, lie within the boundaries of Krka National Park [65]. The study area comprises the upper part of the Krka River estuary and Prokljan Lake (Figure 1b,c, Supplementary Video S1).

The Krka River waters are characterized by low concentrations of nutrients [66] and an extremely low input of terrigenous material [65]. The river is supersaturated in carbonate, enabling tufa barrier formation [31]. Due to the existence of lakes and barriers upstream, the input of terrigenous material is limited. Most of the terrigenous material in Prokljan Lake is sourced by Eocene marls from flysch beds. It is brought by the Gudučа River, which flows into Prokljan Lake from the northeast [67] (Figure 1b).

The Holocene transgression formed a karstic salt-wedge-stratified estuary, where the freshwater or brackish surface layer moves seawards and a bottom seawater layer moves upward as a countercurrent [28,67]. The upper thin water layer (up to 2.5 m) is nearly homogenous and freshwater, with a salinity of 0.2% [28,64]. The bottom seawater layer is separated by a strong halocline, and the salinity reaches up to 37.5% during summer [64] (Liu et al., 2019). The estuary covers a relatively narrow part of the submerged river canyon between the last active tufa barrier (Skradinski Buk waterfalls) and the two wider parts: Prokljan Lake and Šibenik Harbor [68]. The estuary depth gradually increases from 5 m at Skradinski Buk to 43 m at the mouth of the estuary at the entrance of the Sveti Ante Channel. The maximum tidal range is approximately 30 cm at the head and 40 cm at the mouth of the estuary [65]. The sedimentation rate in the upper part of the estuary varies from 1 to 5 mm/year [69,70]. The sedimentation of authigenic carbonate is dominant in the lower part of the estuary (Šibenik Bay), with a sedimentation rate of less than 1 mm/year [30].

Prokljan Lake is situated in the upper part of the estuary and extends in a northwest–southeast direction, covering an area of 11.1 km^2. The lake is 6.7 km-long and up to 2.8 km-wide, and it is connected to the sea by a narrow channel that leads to Šibenik Harbor. The northern part is very shallow, with depths of approximately 1 to 2 m, while the southern part is deeper, with depths up to 25 m. Based on the bathymetry, the paleo-Krka River canyon can be traced from Sveti Ante Channel towards the area between the mainland and Zlarin Island, with its mouth at a depth of 65 m.

3. Materials and Methods

3.1. High-Resolution Acoustic Survey

MBES bathymetry and MBES backscatter data were obtained during the survey of Prokljan Lake using a WASSP S3 MBES (Furuno ENL, Auckland, New Zealand), which was side-mounted on a zodiac boat and moving at a speed of approximately 3.5 knots. The MBES operational frequency was 160 kHz, producing 224 beams in a 120°-angle swath. The vessel positional data were provided using a Hemisphere V103 GPS GNSS antenna with SBAS motion corrections. The pitch, roll and heave motions were corrected with a WASSP Sensorbox (Furuno ENL, Auckland, New Zealand) inertial measuring unit (IMU). WASSP CDX software (version 3.9, Furuno ENL, Auckland, New Zealand) was used for the device control as well as recording the MBES data, whereas the postprocessing of the data was performed with BeamworX Autoclean v2020.2 software.

To determine the subsurface geometry of the study area, we conducted a detailed, high-resolution seismic reflection survey with an Innomar SES-2000 Light parametric SBP, chosen due to its capabilities in shallow-water surveys [71]. Sediment penetration up to 50 m can be achieved [72]. In addition, its theoretical resolution is 5 to 10 cm and practical over 10 cm [73]. We used a 6 kHz low-frequency and a 12 kHz high-frequency setup during the whole survey. An SBP was side-mounted on an 8.5 m-long shallow draught vessel. For positioning and motion corrections, we used an Applanix POS MV WaveMaster with a real-time kinematic unit. Vessel speed was maintained at 3.5 knots. For the processing and interpretation of the seismic data, we used GeoSuite Allworks 2021R2 software.

The SSS surveys were conducted using a Humminbird 999ci HD SI combo echosounder with Hummingbird AS + GPS HS precision GPS with a heading sensor. This sonar device emits fan-shaped pulses with frequencies of 80 kHz or 200 kHz toward the seabed. The sonar was side-mounted on a zodiac vessel with an outboard engine moving at speeds of 3.5 to 4 knots. The mosaic was created in ReefMaster 2.0 software.

3.2. MBES Data Analyses

The MBES bathymetry and MBES backscatter data were processed in BeamworX as a 0.5 m pixel ASCII grid for further analysis in ArcGIS with a Spatial Analyst extension (version 10.2.1, ESRI Inc., Redlands, CA, USA). First, we created a 0.5 m-cell-size digital terrain model (DTM) using an MBES bathymetry grid, from which we derived a range of secondary features, such as multidirectional shaded relief, slope analysis, aspect, and curvature. We resampled a 0.5 m DTM into a 10 m-cell-size DEM for curvature, aspect analyses, and vector ruggedness measure (VRM), as we gained better results with a larger cell size.

Slope analysis was calculated using the standard ArcGIS algorithm proposed by [74]. It is relevant in a geomorphological context as an indirect measure of erosion, the stability of sediments, or the acceleration of currents [75]. We calculated the curvature with the standard ArcGIS tool based on the method proposed by [76]. In addition to the curvature, we also calculated the profile curvature and the planiform curvature. Planiform curvature can be useful when defining ridges, valleys, and slopes along the side of the features [77], where results close to 0 indicate that the surface is flat, values from -0.5 to 0.5 indicate moderate relief, while extreme relief has values <-4 and >4. A Benthic Terrain Modeler (BTM) ArcGIS tool package (version 3.0) [78] was used as an additional analysis tool to describe the geomorphic heterogeneity of the study area. To assess surface roughness (or rugosity), we used the BTM tool Vector Ruggedness Measure (VRM). The authors [57] used roughness as a tool to separate coarse substrates from finer substrates. The values calculated with VRM are dimensionless and range from 0 (no variation) to 1 (complete variation). Typical values in natural data are small and reach up to 0.4 [78]. We also used a semiautomatic BTM classification tool called the Bathymetric Position Index tool, which is intended to classify the landscape structure (e.g., valleys, plains, hilltops) based on the change in the slope position at two scales [78]. For broad-scale and fine-scale analysis, we used an inner radius of 31 cells and an outer radius of 51 cells.

3.3. Ground-Truth Survey and Video Survey

A total of 38 grab samples were collected using a Van Veen grab. Locations for the grab samples were selected based on the different morphological features defined according to unsupervised classified MBES and BSE (Figure 2) data. Additionally, at 27 sampled locations, sea bottom videos were taken with a SeaViewer underwater drop camera. A set of additional 10 grab samples was used for accuracy assessment. Data from the upper parts of five gravity cores were also added to the pool of samples for accuracy assessment. To match the value of a grab sample, the grain size for the gravity cores was calculated as an average of the top five centimeters.

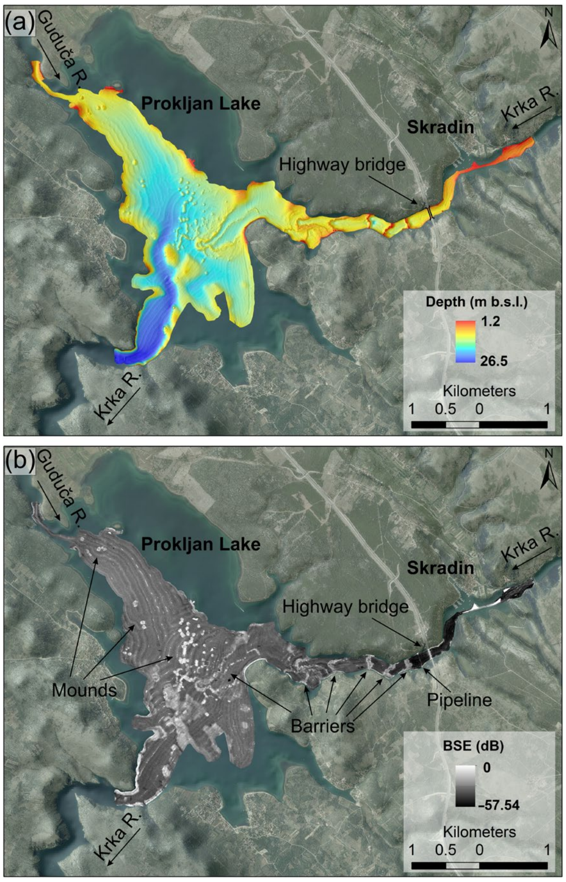

Figure 2. (**a**) Bathymetry map of Prokljan Lake and part of the Krka River estuary representing the results obtained from the MBES survey; (**b**) Map of the same area representing the BSE results.

3.4. Sediment Characterization

The collected grab sediment samples were analyzed for grain size, magnetic susceptibility, mineralogical composition, total organic carbon (OC), total nitrogen (TN), total inorganic carbon (TIC), and insoluble residue (IR) concentrations.

A Shimadzu (Kyoto, Japan) SALD-2300 laser diffraction particle size analyzer was used to analyze the particle size distribution in sediment samples. The instrument measures particle diameters between 0.017 and 2500 µm. First, the organic matter was removed from 0.1–0.2 g of the sample with hydrogen peroxide (H_2O_2) [79]. Since most of the samples in this karst environment are predominantly composed of carbonate material, they were not pretreated with hydrochloric acid (HCl). Fossil shells were manually removed from the samples. Sodium hexametaphosphate ($(NaPO_3)_6$) was added to allow dispersion and prevent particle aggregation. We used GRADISTAT 8 software [80] for statistical data processing. For the sediment classification, the [81] method was applied.

The magnetic susceptibility was measured on powdered samples in 10 cm^3 containers with a Bartington MS2B dual-frequency sensor. The samples were weighed, and the data are expressed as mass magnetic susceptibility (χ_{lf}) and frequency-dependent susceptibility (χ_{fd}%).

To measure OC, TC, TN, TIC, and IR, we used a Thermo Fisher Scientific (Waltham, MA, USA) Flash 2000 NC Analyzer. Two grams of bulk sediment were freeze-dried and ground. The samples were packed into tin capsules for the analysis of TC and TN. To measure OC, the carbonate component was removed by HCl. The TIC was calculated as the difference between TC and OC. The OC/N ratio was calculated by dividing the OC and TN. Insoluble residuum was calculated as the mass difference between the sample treated with HCl and the untreated mass of sediment. The amount of insoluble matter in the sediment was used as a robust measure of the noncarbonate mineral matter in the sediment samples. The analytical precision of this method was controlled by repeated measurements of the individual samples and the standard reference material, Soil NC Reference Material (%N = 0.21 and %C = 2.29).

The bulk mineralogical composition of the powdered sediment samples was determined using a PANalytical X'Pert Powder X-ray diffractometer. It was equipped with Ni-filter CuKα radiation, a vertical goniometer with a θ/θ geometry, divergence and anti-scatter slits of $\frac{1}{4}$, and a PIXcel detector. Data were evaluated with HighScore X'Pert Plus software using the International Centre for Diffraction Data database (PDF-4/Minerals).

3.5. Object-Based Image Analysis

In the OBIA of MBES backscatter data in ArcGIS, we used particle size analysis (PSA) and MBES bathymetry to define the classes. In the relatively recent literature, OBIA is used in the analysis of geospatial data that takes into account not only raster MBES data but also other inputs, such as PSA, geometry, texture, or statistics [58,82,83]. The premise is to use ground-truth data to train the classifier algorithm, which accordingly classifies the whole backscatter raster implicitly. In our case, OBIA consists of three steps: raster segmentation, training a classifier, and finally classifying the raster. First, we segmented the MBES backscatter raster with the Spatial Analyst tool Segment Mean Shift. Segment Mean Shift is a nonparametric clustering method for image segmentation that determines segments in the raster by grouping neighboring pixels with similar spectral characteristics. The number of significant clusters present in the feature space is automatically determined by the number of significant modes detected [84]. In ArcGIS, one can control the amount of spectral and spatial detail and the minimum segment size to derive features of interest. As a second step, we created a training point feature based on grab sampling locations and PSA. PSA classes were determined based on the Folk and Ward [81] classification in GRADISTAT 8 software [80], and two sets of classified maps were created, with four and seven classes, respectively. This training feature was used to train the random tree classifier. The ArcGIS random tree classifier is a "black box" method with no detailed description of the method, so only the general methodology can be described. The random tree is a machine-learning tree-structured stochastic classifier. A collection of such classifiers makes a random forest. This is an effective tool for prediction and a very accurate classifier [85]. According to [7], random forests are fast in training and testing but slow and time-consuming in the preprocessing stage. They allow for various descriptors to be easily combined [86]. After classification, the final step in the process was to classify the segmented raster based on the previously trained classifier. In addition, an MBES bathymetry set was used as an ancillary dataset to generate better attributes for classification.

The overall accuracy assessment and Kappa coefficient of agreement of the dataset were calculated within the ArcGIS environment. The confusion matrix was created based on an additional set of samples not used for classification, comprising 39.47% of the initial sample set used for classification. The overall accuracy assessment is a percentage value of accurately detected cases. It is calculated as the number of accurately detected cases divided by the total number of ground-truth samples [82]. Kappa is a measure of agreement on the probability that the mapped pixel is attributed to the correct class [57,82].

4. Results

The obtained MBES, BSE, and SSS results of the analyses of collected sediments and videos with GIS analyses and classification tools were used to define the seabed geomorphology of the area.

4.1. Seabed Morphology Determined with Geophysical Acoustic Methods

MBES and SSS surveys were conducted covering the bathymetric depth range of approximately 5–26.6 m below sea level (b.s.l.), with a mean value of 14.7 m b.s.l. (Figure 2). The coastal areas within Prokljan Lake were too shallow to efficiently map. Consequently, an area of approximately 6 km^2 of the seabed was surveyed. The MBES backscatter (BS) intensity ranged from −16 dB to −57 dB for 99.9% of the collected data (Figure 2b). The backscatter physiography of the survey area consisted of low, acoustic backscatter surfaces on the flat bottom, while the well-defined barriers, mounds, and canyon sides exhibited high surface backscatter responses.

The studied area can be subdivided into two morphologically distinct areas: the Krka River canyon, with elongated geometry and steep slopes, and the wide Prokljan Lake, with a relatively flat bottom. The shallowest part lies at the northeastern end of the canyon (Figure 2a). In front of the town of Skradin, the water depth is lower than 5 m. This is also the area where the lowest backscatter values, below −35 dB, are found. Sediments with low backscatter values spread downstream around the highway bridge. The region directly below the highway bridge shows a very strong backscatter response, with values of −25 to −28 dB. Downstream of the bridge lies the detected pipeline, also with strong backscatter surrounded by areas of low backscatter response. The canyon deepens in its central part, where average depths reach 10 m b.s.l., while at its end, where the canyon meets Prokljan Lake, depths reach 13–15 m b.s.l. The shallowest part of Prokljan Lake is on the northern side, where the Guduča River meets Prokljan Lake, with depths of approximately 12 m b.s.l. The Prokljan Lake bottom deepens toward the exit into another part of the Krka River canyon in the SW part of Prokljan Lake (Figure 2a). The depths at the exit reach up to 25 m b.s.l. An incised canyon, oriented from north to east, can be tracked in Prokljan Lake from its central part toward the exit from Prokljan Lake (Figure 2a). The incised valley is bounded on both sides by carbonate rocks extending from the land. The promontory protrudes into the lake from the south toward the center of the lake.

A series of submerged barriers are visible in the central and western parts of the canyon, extending into Prokljan Lake (Figures 2 and 3). Barriers are elongated, extending from one canyon side to the other. They are 150 m to 2000 m long and approximately 50 m to 100 m wide at the base, thinning upward to only several meters at the top (Figure 4). The most eastern (or most upstream) barrier (Barrier 1, Figure 4) is located in the central part of the canyon, 350 m east of the highway bridge. The barrier grew perpendicular to the canyon. Its depth at the crest is approximately 4.6 m b.s.l. There are two distinct 9-to 11 m-wide gaps in the central-to-southern part of the 150 m-wide barrier (Figure 4, B1). The bottoms of the gaps reach 8 and 9 m b.s.l., respectively. Approximately 200 m downstream is the second barrier (Barrier 2, Figure 4, B2). The crest reaches a depth of 4.6 m b.s.l. in the centerline and features gaps in the central-to-southern part of the barrier, whose bottoms reach depths of 9.1 m b.s.l. Further downstream by 250 m lies the third barrier (Barrier 3, Figure 4, B3). Its centerline is slightly S-shaped and 250 m long, with two 10–15 m-wide gaps and a 65 m-wide opening. The bottoms of the gaps are at 7.6 and 8 m b.s.l., while the bottom of the wide opening reaches 8.2 m b.s.l. The barrier crest is located at 4.6 m b.s.l. Barriers 1, 2, and 3 are detected as areas of high BS response, with values of −25 to −30 dB. The fourth barrier is located approximately 500 m downstream (Figure 4, B4). This barrier is U-shaped, with a tip pointing in the Krka River flow direction toward Prokljan Lake. Its total length over the centerline is more than 400 m, and it has a very irregular surface (Figure 4, B4). Therefore, it is difficult to determine the crest depth, which ranges from −8.2 m b.s.l. to −10 m b.s.l. At a distance of 75 m or more, there is another U-shaped barrier (Barrier 5, Figure 4, B5). This barrier is more complex and is actually a system of (at least) five barriers that branch out in the central to the southern part. The longest centerline over the crest is more than 750 m-long, with an irregular surface (Figure 4, B5). The depth in the northern-to-central part of the barrier varies from 8.6 m to 9 m b.s.l., and in the southern part, it varies from 9.5 m to 10 m b.s.l. There is a 15 m gap in the northern tip of the barrier, reaching a depth of 10.5 m b.s.l. Backscatter of Barrier 4 and the more complex Barrier 5 is not as pronounced in the surrounding low BS response medium but can still be very successfully traced. The final prominent barrier starts 500 m to the west and extends from the Krka River canyon into the wide Prokljan Lake (Barrier 6, Figure 4, B6). The basin formed by the barrier is divided in the middle by a smaller barrier. It has a prolonged U shape, with a length over the crest centerline of almost 2000 m. The surface is irregular, and the crest depth varies from 11.2 m to 13.3 m b.s.l. (Figure 4, B6). The crest depth of the more than 900 m-long barrier in the central area of Barrier 6 varies from 12.6 m in the NE part to 15.2 m b.s.l. in the southern part. Two additional barriers branch out from Barrier 6 toward the south and west. The southern branch is partially preserved, with a crest depth of 14.5 m b.s.l. and a large opening reaching 17 m b.s.l. The eastern branch is better preserved, and its crest varies from 13.5 m to 14.5 m b.s.l. The backscatter response of the complex Barrier 6 is partially even less pronounced than Barriers 4 and 5, but some parts have a strong BS response, varying from −25 to −29 dB. Only 50 m to the east is the final barrier (Barrier 7, Figure 4, B7), which is located on the edge of the incised valley. It lies at depths of 15 to 16 m b.s.l. Several mounds lie to the north of Barriers 6 and 7. Some, especially those closer to the preserved barriers, can be delineated (Figure 4, B8). The tips of the mounds lie at depths of 13.5 m b.s.l. to 14.3 m b.s.l. The round mounds have a very contrasting backscatter response compared to the surrounding low-BS-response medium. They have a very high response, reaching −22 dB. There are several mounds located toward the Guduča River inlet. They have a slightly weaker response than those in the central part of Prokljan Lake. The shallower area in the southern part of Prokljan Lake is characterized by a stronger BS response (Figure 2b). That area extends from the south toward the center of Prokljan Lake, reaches Barriers 6 and 7 and is bound by the valley toward the exit from Prokljan Lake (Figure 2b).

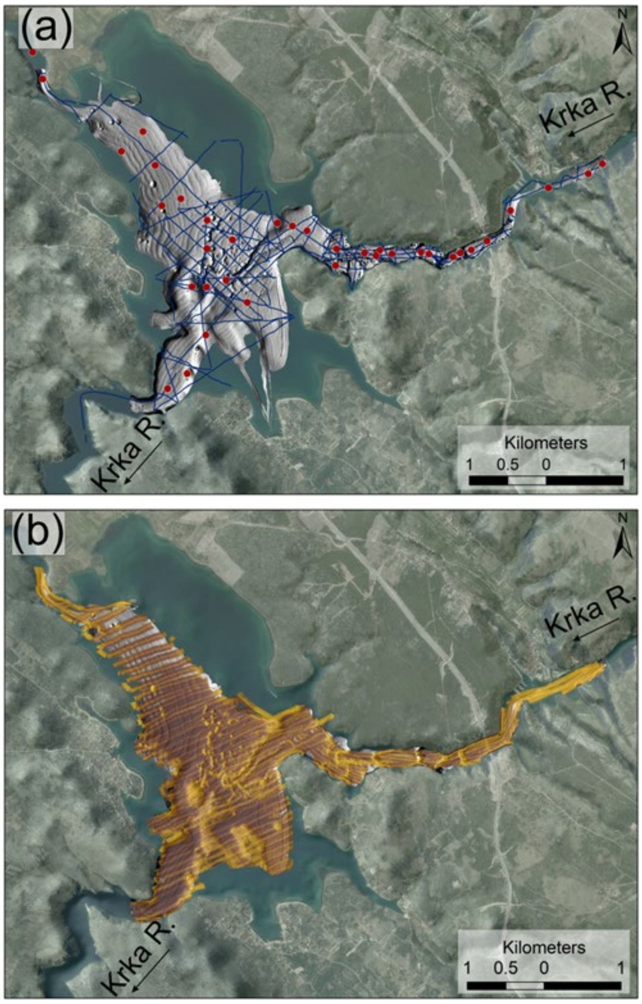

Figure 3. Maps representing the results obtained from (**a**) multidirectional hillshade based on MBES data with plotted sampling locations (red dots) and SBP tracklines (blue lines) and (**b**) SSS survey data.

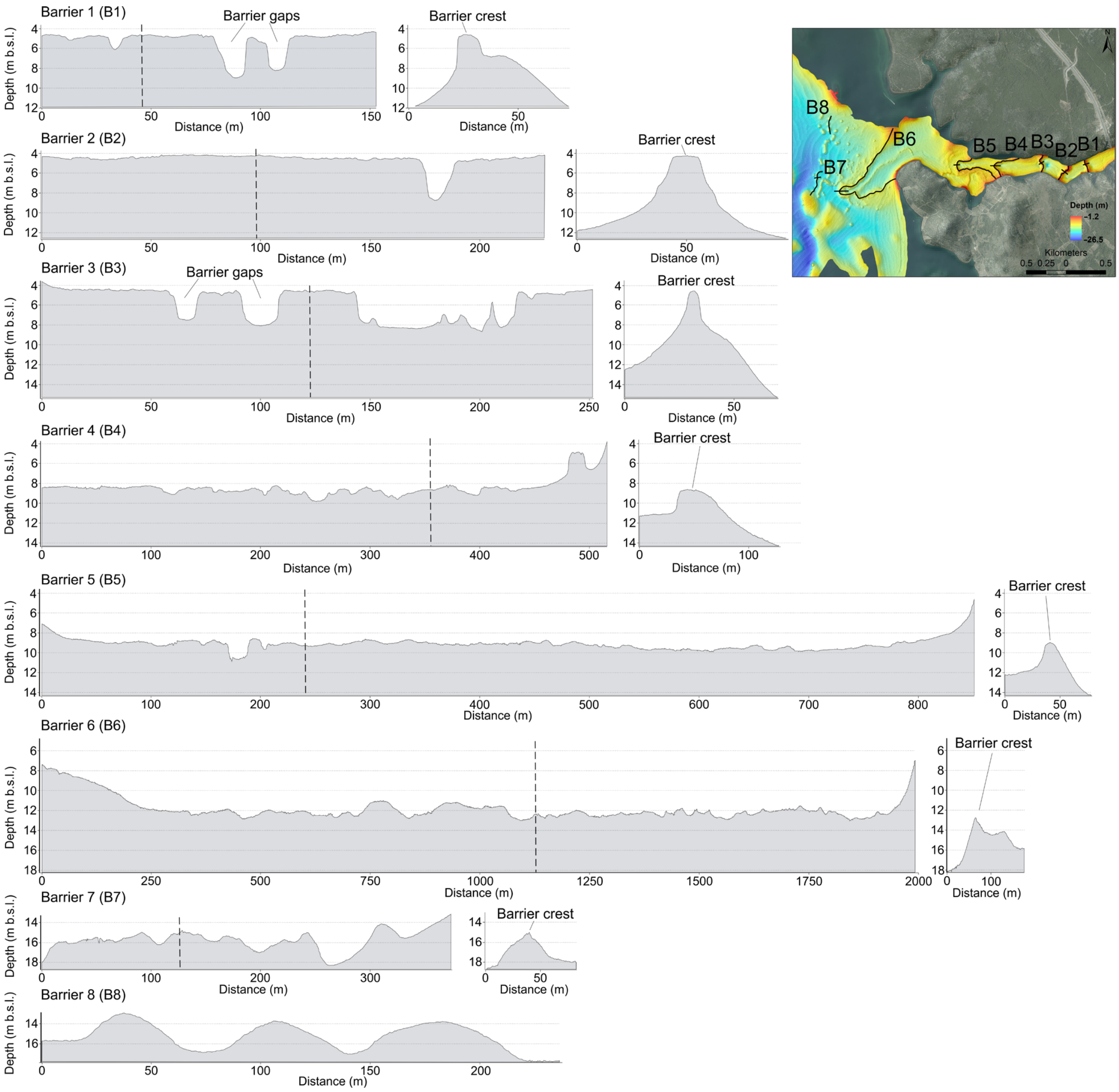

Figure 4. Profiles of selected barriers in the study area representing their shapes and depths. Long profiles are located along the crests of the barriers. Short profiles next to long profiles are perpendicular to long profiles. Locations of perpendicular profiles are marked with the dashed line on the long profile. The horizontal scale varies.

A visual analysis of the SSS mosaic was used to aid in the interpretation of the geomorphological characteristics of the MBES and SBP data. The upper part of the Krka River canyon around Skradin has a uniform bottom with higher reflectivity (Figure 3b). As the canyon develops steeper sides downstream of Skradin, bottom reflectivity decreases. Downstream of the highway bridge, there is a linear pipe element visible at the bottom, and 150 m downstream, the first barrier is visible. It is characterized by a high reflectivity of the SSS mosaic. The mosaic also shows a very irregular and rough surface of the barrier crest. Downstream of the barrier, the bottom is uniform with low reflectivity, reaching the next barrier with high reflectivity. The SSS mosaic shows that Barrier 2 branches in the northern part into two parts. A similar pattern of low-reflectivity flat sediments and high-reflectivity barriers can be tracked through the whole canyon (Figure 3b). A similar pattern can be observed in Prokljan Lake, where high reflectivity is appointed to the barriers, mounds, and rocky sides of Prokljan Lake, while flat bottom sediments cause low reflectivity in the mosaic. The darkest hues can be observed in the incised valley toward the exit from Prokljan Lake.

4.2. MBES Bathymetry Analyses Results

The slope analysis performed on the MBES bathymetry data ranged from zero degrees to 75.3 degrees (Figure 5a). We additionally reclassified the slope analyses raster into four classes (0–5°, 5–20°, 20–40°, and >40°) to obtain a better statistical overview of the slope coverage in the studied area. The results show that 77.3% of the area has a slope inclination lower than 5°, while 21.8% of the area has a slope inclination in the range of 5–20°. Steeper slopes are rare and mainly cover the sidewalls of the valley at the exit from Prokljan Lake and parts of the barriers. Slopes in the range of 20–40° cover 0.8% of the surveyed area, and slopes over 40° cover 0.04%. Aspect analysis shows a uniform distribution of the slope direction throughout the area of interest. North-facing slopes cover the lowest amount of the study area, comprising 8.7%, and NW slopes cover 10.3% of the area.

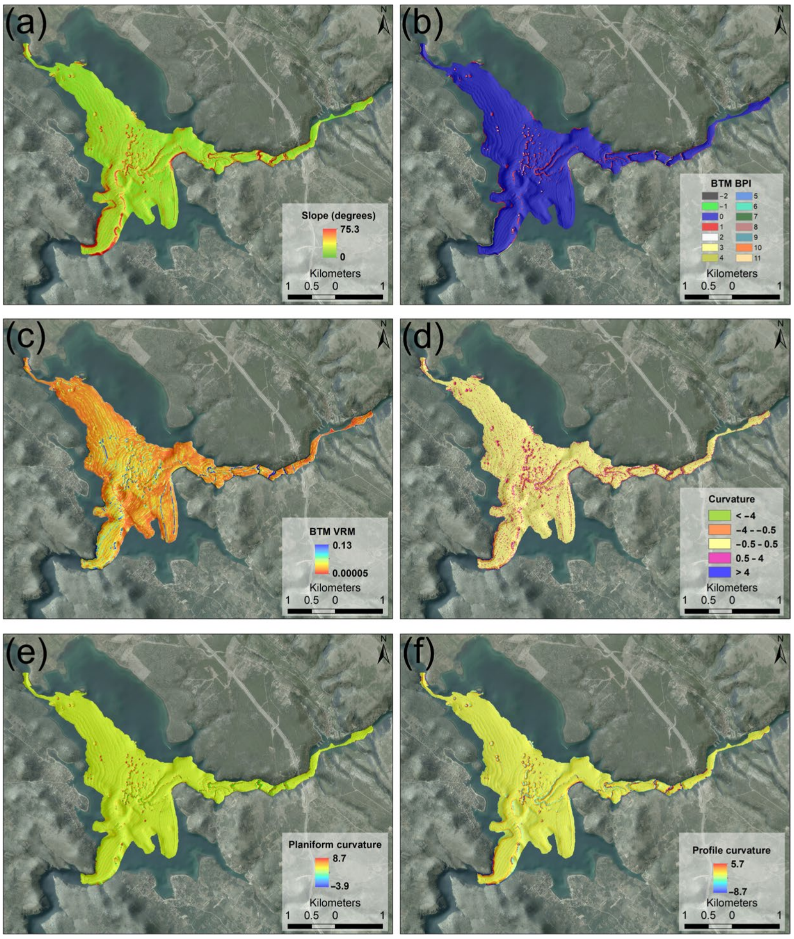

Figure 5. (**a**) Slope analysis of the study area; (**b**) Bathymetric Position Index; (**c**) Vector ruggedness measure; (**d**) Curvature analysis of the study area; (**e**) Planiform curvature calculated for the study area; (**f**) Profile curvature calculated for the study area.

A BTM tool, the Bathymetric Position Index, was successful in the classification of plains and ridges, with almost identical results in broad-scale and fine-scale analyses (Figure 5b). The dominant class defining plain areas (Class 0, Figure 5b) covered more than 94.4% of the total area, while classes defining ridges (Classes 1 and 2, Figure 5b) covered 4.3% and 0.7%, respectively. Surface roughness was analyzed with a BTM tool VRM. The tool managed to define areas with coarser sediments and separate them from areas with finer-grained material (Figure 5c). Better separation was achieved with the analysis of the 10 m-cell-size DEM, where barriers and mounds were defined as areas with higher variation, reaching a maximum value of 0.138 for a 0.5 m cell size and 0.02 for a 10 m cell size.

The curvature analysis of the 10 m-cell-size DEM showed high relief (orange and purple colors, Figure 5d) in the valley sides at the exit from Prokljan Lake and around mounds and barriers. The dominant part of the investigated area (85%) has moderate relief with calculated values within the range of −0.5 to 0.5, while high relief (−4 to −0.5 or 4 to 0.5) covers 14.7% of the area. Extreme relief was detected in only 0.3% of the area. The planiform curvature meant to emphasize convex or concave forms in the relief, such as ridges, valleys, and slopes, successfully delineated mounds and barrier crests that stand out on the map in orange and reddish hues, with values above 0.7 (Figure 5d). The profile curvature, designed to stress acceleration (or deceleration) of the flow, defined barriers and mounds as the areas of deceleration, with negative values at crests and elevated values at the base, while most of the analyzed data showed low values (Figure 5e).

4.3. Sub-Bottom Profiler Survey

We used the high-resolution seismic survey in the study area as an aid for a better geomorphological interpretation of the bottom. With this goal in mind, we made a detailed grid comprising 128 acoustic profiles with a total length of 89.6 km. The acoustic signal penetration into the sediment was up to 16 m. Due to a relatively shallow water depth, the multiples masked deeper parts of the profiles.

The sedimentary sequence of the Krka River and Prokljan Lake in the seismic profiles can be divided into four major seismostratigraphic units. The upper seismic unit (Unit 1, Figure 6) is acoustically homogenous and transparent. Unit 2 has similar characteristics and is separated from Unit 1 by a high-amplitude reflector composed of a series of hyperbolae. The lower part of Unit 2 exhibits parallel reflectors with weak amplitudes. Unit 2 and Unit 3 are divided by an erosional boundary. Unit 3 is the lowermost unit (Figure 6) with high-amplitude subparallel reflectors. Due to the effect of the multiple reflections, the bottom of Unit 3 is not clear. Unit 4 can be described as a nontransparent unit, mainly protruding from the surrounding units. Due to its nontransparent properties, it is not possible to determine the base of Unit 4. Although Unit 4 protrudes mainly to the surface, sometimes it is covered by a thin drape of Unit 1. Additionally, in the case of the area near Barrier 6, Unit 4 is covered by Units 1, 2, and 3.

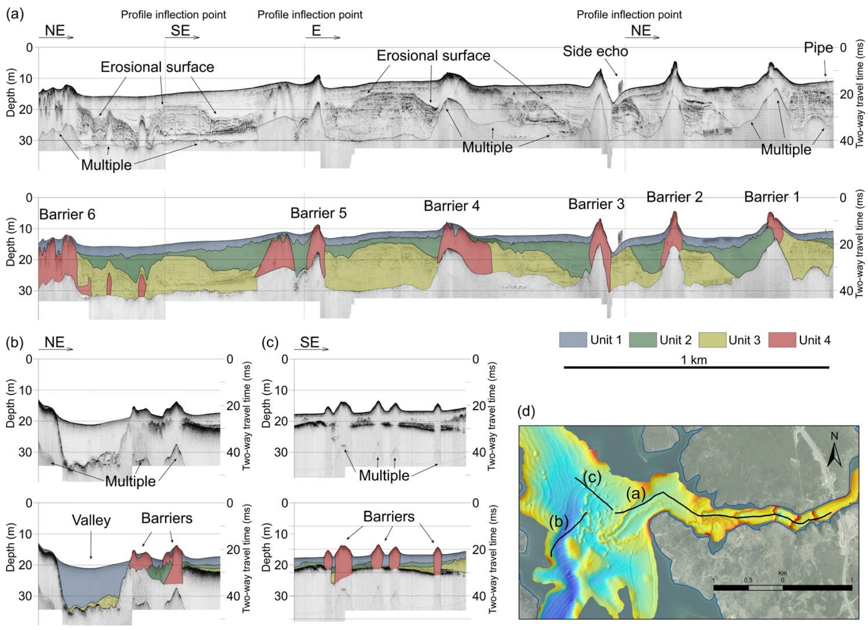

Figure 6. High-resolution seismic profiles showing the morphology of the study area. (**a**) Long SBP cross-section passing over barriers and adjoining sediments; (**b**) SBP cross-section presenting submerged tufa barriers and a filled river canyon; (**c**) SBP cross-section through carbonate mounds and adjoining sediments; (**d**) map with tracklines of presented SBP profiles.

The profile presented in Figure 6 a was created by merging three longitudinal profiles to obtain the best overview of the sub-bottom morphology of the studied area.

4.4. Sediment Characterization

4.4.1. Sediment Particle Size Fractions

The collected sediment samples were predominantly classified as silt and sand [81] (Figure 7d). The mean particle sizes range from fine silt to coarse sand (4.5–575.6 µm). The distribution of the particle size of surface sediments is shown in Figure 7d, and the results of the granulometric analysis are presented in Supplementary Table S1. Medium to coarse silt is the dominant type of sediment in the upper part of the estuary, near the city of Skradin. The tufa barriers, carbonate mounds, and shallower parts of Prokljan Lake are mainly composed of medium silt to coarse sand. Deeper water estuarine parts of the lake are predominantly composed of fine to medium silt. The distribution of silty samples is unimodal, and they are poorly sorted, whereas the sandy samples have bimodal or trimodal distributions and are very poorly sorted.

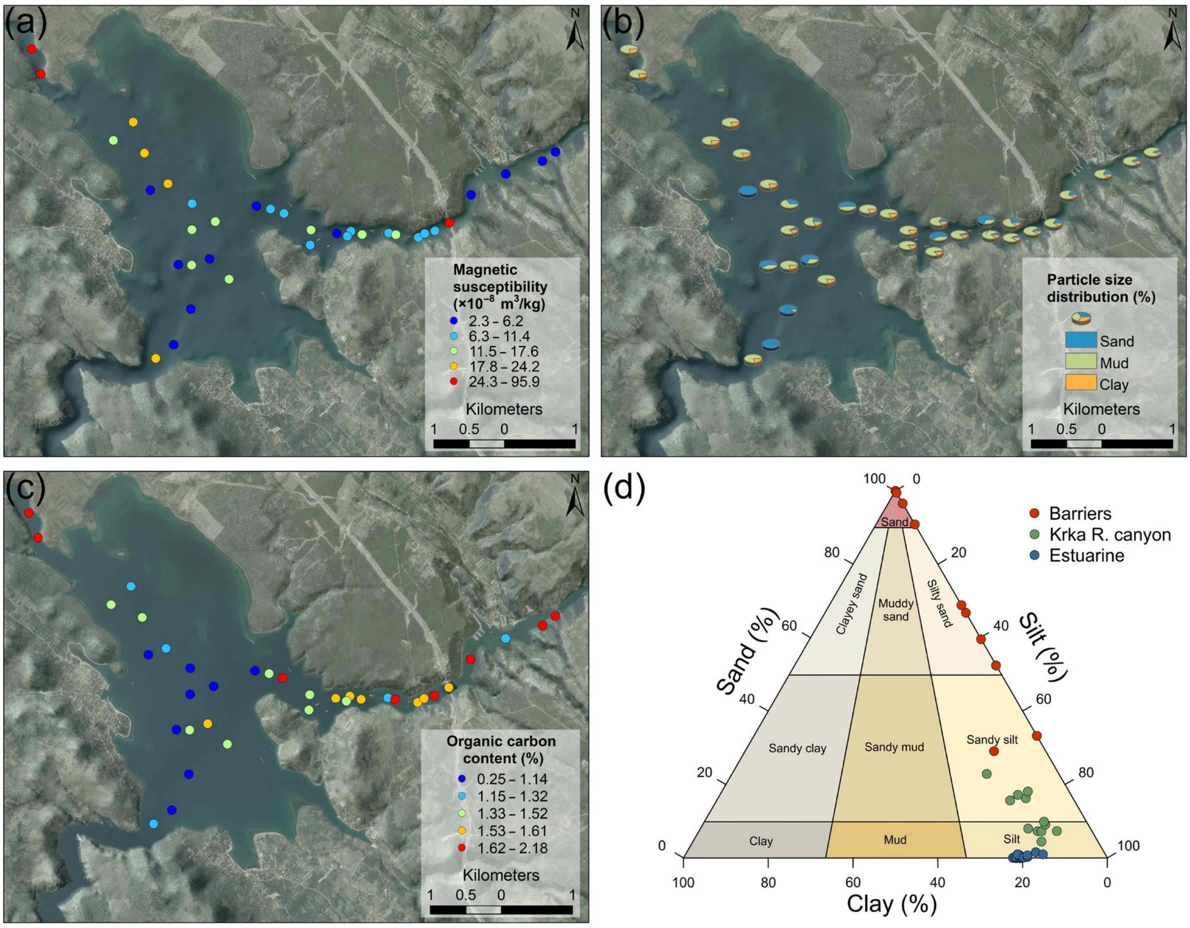

Figure 7. (**a**) Distribution of grab samples and magnetic susceptibility (χlf) measured in sediments; (**b**) particle size distribution (in %) of sampled sediments; (**c**) distribution of organic carbon content in sampled sediments; (**d**) Ternary diagram showing the distribution of samples' particle size according to their locations in the survey area: barriers and mounds (red), Krka River canyon (green), or plain estuarine areas of the survey area (blue).

4.4.2. Mineral Composition

The mineral composition of the grab samples was made of carbonate and noncarbonate fractions. The carbonate fraction was composed of calcite, aragonite, magnesium calcite, and dolomite. The noncarbonate fraction contained quartz, halite, muscovite/illite, kaolinite, and amphibole. The major mineral phase in all surface samples was calcite. Along with calcite, the dominant minerals in samples PJ-15, PJ-29, and PJ-30 were aragonite and magnesium calcite. The two most important accessory minerals occurring within the samples from the tufa barriers and carbonate mounds were aragonite and magnesium calcite.

4.4.3. Magnetic Susceptibility

The mass magnetic susceptibility values of the grab samples in the study area ranged from very low values of 2.3×10^{-8} m^3/kg to moderate values of 26.1×10^{-8} m^3/kg, with an average of 13.3×10^{-8} m^3/kg. A significantly higher magnetic susceptibility value of 95.9×10^{-8} m^3/kg was measured in sample PJ-19, which was retrieved under the highway bridge (Figure 7a). Magnetic susceptibility values varied between 0 and 9.2%. The lowest magnetic susceptibility values, $<5.1 \times 10^{-8}$ m^3/kg, were recorded in 10 samples taken from tufa barriers, carbonate mounds, and the shallow uppermost part of the study area. Magnetic susceptibility values ranging from 5.1 to 17.6×10^{-8} m^3/kg were measured in 29 samples retrieved from the central deeper parts of Prokljan Lake and the small lakes behind the barriers. Values higher than 17.6×10^{-8} m^3/kg occurred in seven seabed samples located in the NNW part of Prokljan Lake, where the Gudubča River enters the lake, and at the exit of Prokljan Lake (Figure 7a).

4.4.4. Carbon and Nitrogen Analyses

The distribution of organic carbon in the study area is shown in Figure 7c, and the OC, TIC, TN, TC, IR and OC/N results are summarized in the Supplementary Table S2. The OC values range from 0.25 to 2.18%, with a mean of 1.36%. A lower OC content (lower than 1%) was measured in the samples taken from tufa barriers and carbonate mounds, while values >1% were recorded in the muddy sediments from the deeper part of the estuary (Figure 7c, Supplementary Table S2). The TIC values range from 1.84 to 7.95%, with a mean of 3.99%. The TN contents vary between 0.05% and 0.28% and show a similar pattern to that of the OC content. The organic carbon-to-nitrogen ratios (OC/N) range from 4.5 to 8.85.

4.4.5. Seabed Classifications Based on MBES Bathymetry Analyses

We paired MBES backscatter data with the classified results of the sediment PSA. This pairing enabled us to create OBIA maps of sediment PSA distribution divided into four or seven classes. A four-class map is classified into silt, sandy silt, silty sand, and sand (Figure 8a). Most of the studied area is covered by silt (84.8%). The area covered with sediments classified as sandy silt is 4.1%, while the area covered with silty sand equals 7.3%. Finally, the sand class covers 3.1% of the studied area. The dominant particle size in the seven-class Folk and Ward (1957) classification is fine silt, which covers 77.6% of the area (Figure 8b). Among the other silt subclasses, medium silt covers 10.1%, coarse silt covers 0.9%, and very coarse silt covers 0.8%. Among the sand-sized fractions, the largest area is covered by very fine sand (8.1%), while medium sand covers 2.2% and coarse sand covers 0.3% of the entire study area.

Overall accuracy assessments were made for both classifications. A fairly simple four-class classification map had a satisfactory accuracy assessment of 93.3%, while a more complex seven-class map had a lesser accuracy assessment of 86.7%. Respective Kappa coefficients ranged from 0.9 for a four-class classification, and 0.83 for a seven-class classification. As the majority of the studied area is covered by silt in a four-class classification, it is important to stress that the accuracy assessment for this class was 100%, while it was lowest for sand (75%). In a seven-class classification map, there is also one dominant sediment type, a fine silt, that also has an excellent accuracy assessment, but it was lower for classes of medium silt and very coarse silt with values of 67%. A limited discriminatory power of backscatter data between different coarse sediment classes is visible in a seven-class map (Figure 8b). Very coarse silt, medium sand, and coarse sand are virtually indistinguishable based only on MBES backscatter. This stresses the need for secondary inputs besides MBES backscatter and MBES bathymetry data to achieve the most accurate results in the definition and segmentation of seafloor classification [12,57]. The reason for the effect is probably a low number of samples for specific substrate types.

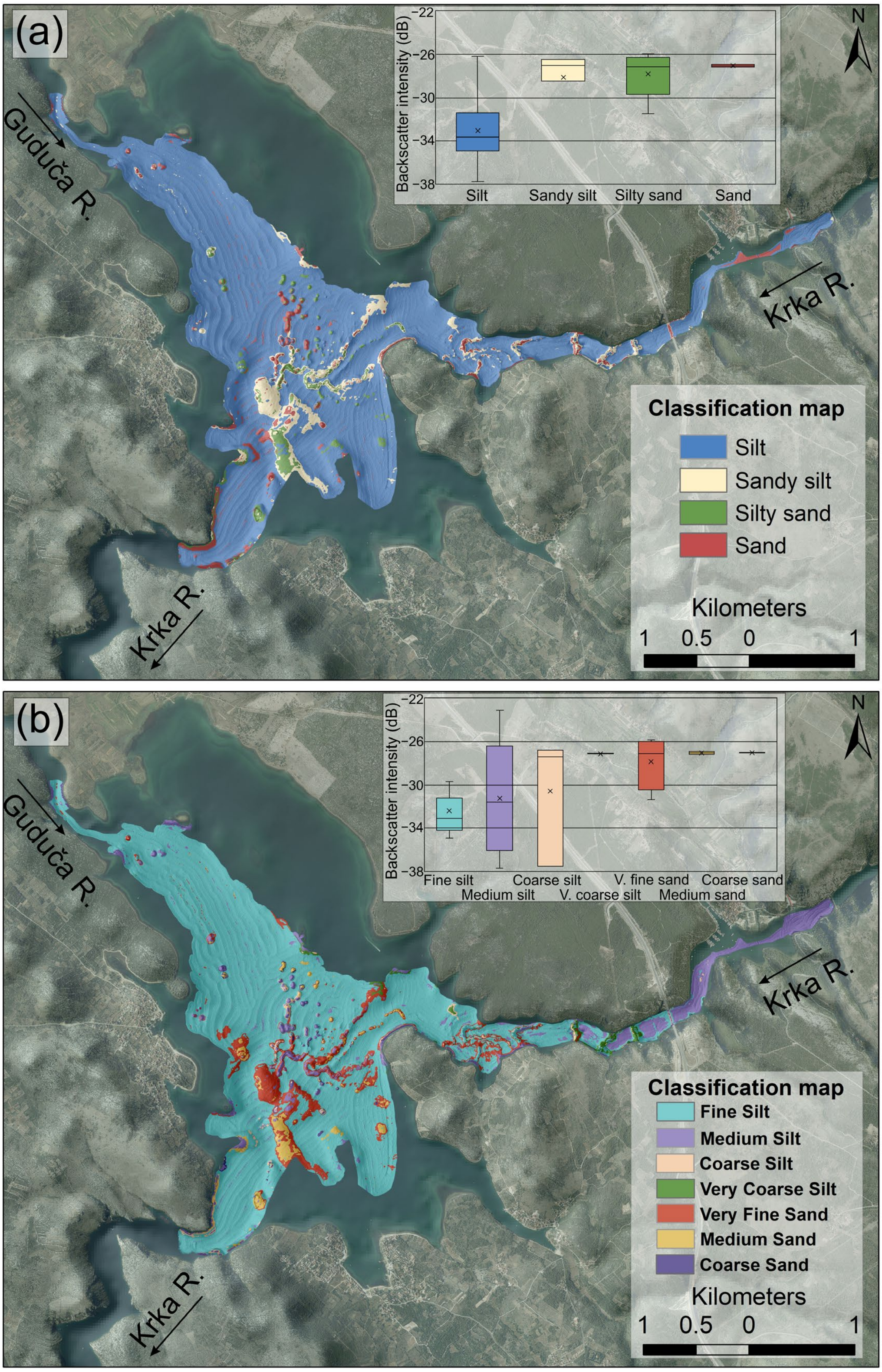

Figure 8. Map of the sediment distribution in the study area based on the OBIA of the MBES backscatter data and PSA, classified into (**a**) four classes and (**b**) seven classes. The distribution of the mean backscatter intensity in classes is shown on box-and-whisker plots.

5. Discussion

The studied part of the Krka River estuary consists of two distinct morphological parts: a narrow, submerged Krka River estuary canyon and a wider Prokljan Lake. Both comprise distinct geomorphological features, specifically submerged tufa barriers and carbonate mounds typical of the karst surroundings. They also act as sediment traps, keeping a portion of the sediment behind them. By the integration of the morpho-bathymetric surveys (MBES, BSE, and SSS) and acoustic SBP profiling, with the addition of ground-truthing and many sediment sample analyses, we managed to create a precise OBIA, interpret and classify data into maps with good confidence, and recreate the geomorphological evolution of the area. The depth of each detected barrier in the Krka River estuary, in connection with the onset of marine sedimentation within the estuary, can be used as a sea-level indicator since barriers stop growing if they are flooded.

5.1. Sediment Composition and Dynamics

The Krka River is characterized by relatively low terrigenous sediment input in the estuary [65] given its karstic watershed, but also due to the tufa barriers located upstream of the estuary, thus preventing sedimentary input. Marine sediment transport is also very low because of the salt-wedge type of the estuary, small wave actions, and weak bottom currents and tides [16,17]. Therefore, it can be assumed that the main source of the terrigenous supply in the lower Krka River estuary is the Gudača River, whose catchment area is built of flysch deposits [63]. Additionally, the lack of tufa barriers within the Gudača River enables the transport of the material. From the particle size distribution map of surface estuary sediments (Figure 8), the decrease in particle size with increasing depth can be distinguished. The largest amount of silty sediment was deposited in the paleochannel of the Gudača River on the western side of Prokljan Lake, but also near the Gudača River mouth and in the southern outlet of Prokljan Lake (Figure 8), where the paleo-Krka and paleo-Gudača rivers incised the canyon toward the city of Šibenik. The upper part of the Krka River canyon bottom is built of sandy silt. Sediment on the tufa barriers and carbonate mounds is composed of silty sand to coarse sand. The sand particles are mainly of biogenic origin (shells and fragments of benthic organisms). The bimodal or polymodal particle distribution and the poor to very poor sorting of sediments point to more than one source of sediments and a mixture of terrigenous and biogenic particles.

This is also supported by the mineral composition. The main mineral in all the surface sediments is calcite. In the fine-grained fraction, terrigenous quartz and clay minerals are also present, originating mainly from parts of the catchment with Eocene marls and, to a lesser extent, from the erosion of the thin soil cover that sparsely covers the karst. In the sand fraction from tufa barriers and carbonate mounds, aragonite and high-magnesium calcite are dominant, along with calcite, indicating biogenic origin. Insoluble residuum and magnetic susceptibility show a weak negative correlation with the backscatter intensity of silt samples (Figure 9).

Magnetic susceptibility values correlate very well with the grain size distribution and insoluble residuum, which were both used as a robust measure of the siliciclastic content of the sediments (Figure 9). The highest value was found in the sediment below the highway bridge and, therefore, can be associated with anthropogenic activity due to road runoff (drainage from the bridge). Slightly elevated values were detected on the western side of Prokljan Lake, near the Gudača River ($>20 \times 10^{-8}$ m^3/kg) and in the southern outlet of Prokljan Lake. These samples were also characterized by a higher percentage of frequency-dependent magnetic susceptibility ($\lambda fd > 8\%$), which indicates the presence of ultrafine superparamagnetic magnetite minerals, found commonly in soils [87]. This corresponds to the terrigenous supply and higher siliciclastic content in these samples.

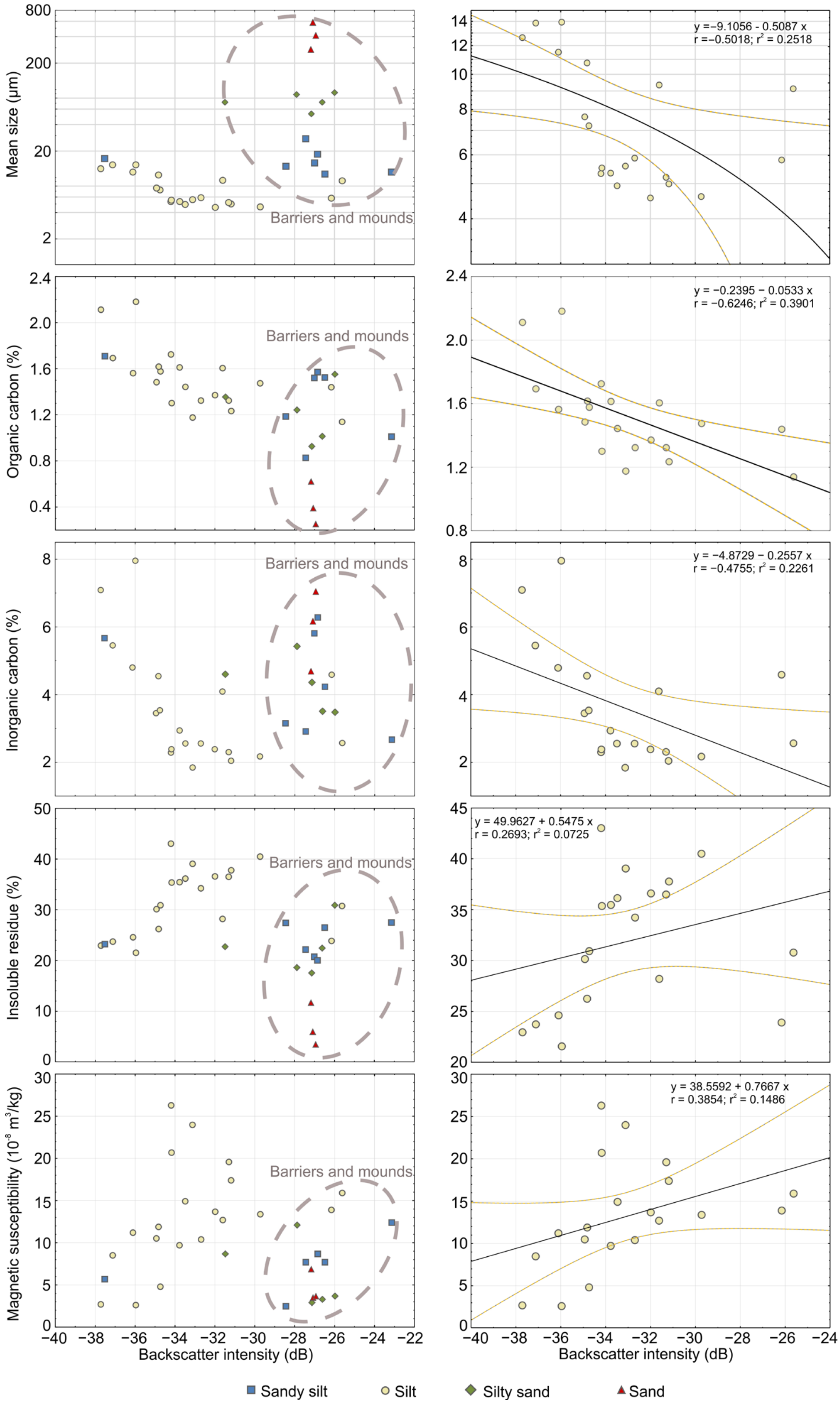

Figure 9. Values of backscatter intensity compared with mean grain size (µm), OC (%), IC (%), IR and magnetic susceptibility (10^{-8} m^3/kg). Scatterplots in the left column are made for all grab samples grouped by the sediment type. Scatterplots in the right column represent silt-sized samples and their correlation with variables. Gray ellipses represent the distribution of samples mainly from barriers and mounds. Yellow dashed lines represent the 95% confidence interval.

Many studies on the distribution of organic matter in surface sediments have shown a direct relation between OC and the particle size distribution and mineral composition of surface sediments (e.g., [53–56]. The linear regression results for mean backscatter (dB) and OC (Figure 9) fit a linear model for the mud sediments (r = 0.62), but no correlation exists with the coarse carbonate sediments derived from disintegration of the submerged tufa barriers and mounds (Figure 8). The correlation between sediment OC and mean backscatter (dB) allowed the construction of a predicted distribution map of OC in the estuary (Figure 10) based on the correlation equation calculated for the mud-sized fraction (Figure 9). The distribution of OC depends on the morphology of the Krka River estuary, with the highest concentration of OC in the small basins between individual submerged tufa barriers in the canyon part of the estuary. Although the energy and hydrodynamics in the estuary are low [65], the OC distribution in the sediments is generally higher along the main current of the Krka River, and decreases seaward (Figure 10). The highest OC concentrations ranging from 1.17 to 2.18% were present in the silt samples (containing a higher content of clay) located in the Krka River canyon, near the town of Skradin, and in samples taken at the mouth of the Gudača River. Both areas are located in catchments that contain highly erodible Eocene flysch deposits (marls) and arable lands. The highest concentrations may be related to anthropogenic activity and/or higher sedimentation rates [30,53]. In the central part of Prokljan Lake, where the sedimentation rates are the lowest, the concentrations of OC are also low. The lowest concentrations of OC (<1%) were recorded in sandy samples composed of calcite, aragonite, and high-magnesium calcite (PJ-15, PJ-29, and PJ-30), which were sampled in the vicinity of submerged tufa barriers and mounds. The rest of the silty samples that contained higher clay fractions had higher OC concentrations (>1%). The distribution of organic matter is closely associated with fine-grained sediments [88,89] and high sedimentation rates [53], even though other significant factors, such as bioturbation and bottom-water oxygen levels, can influence the distribution of organic matter ([90] and references therein). TN concentrations and their spatial distribution also correlate very well with OC values (r = 0.96), thus indicating a common organic source [91].

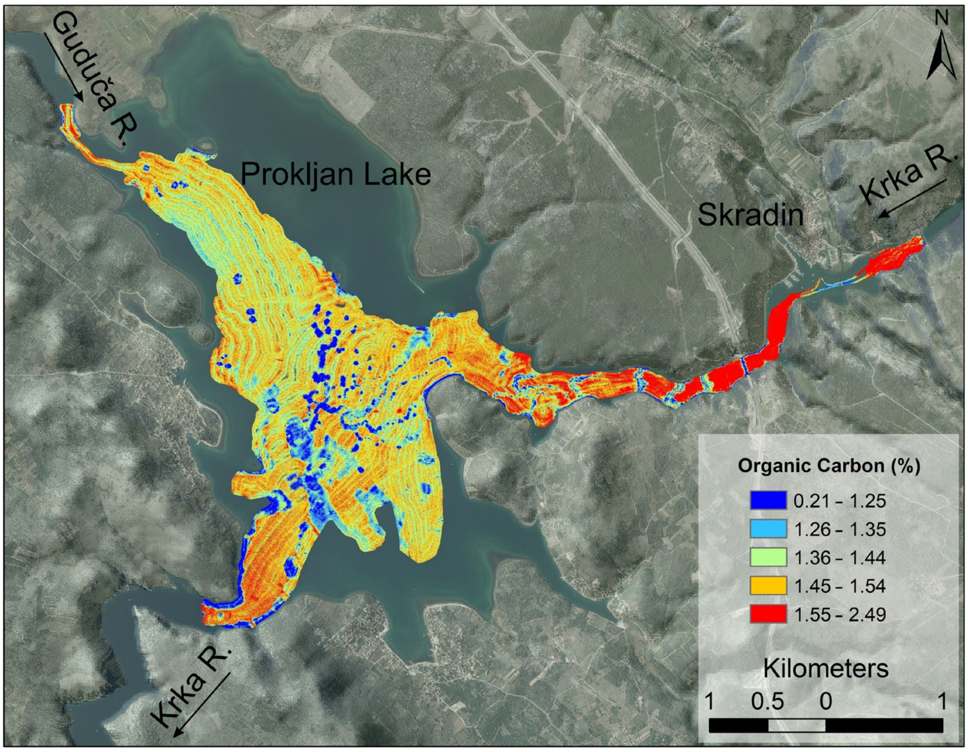

Figure 10. Predicted distribution of organic carbon (%) based on the correlation equation calculated for the silt-sized fraction.

The OC/N ratio is often used as an indicator of sources of organic matter in marine and lacustrine environments [54,92] and as a tool for distinguishing algal matter from higher-plant matter [54]. The OC/N ratios in sediments with an algal origin or pelagic source have OC/N ratio values between 4 and 10, whereas OC/N ratio values for higher plants are higher than 12 [54]. Some authors have implied a terrestrial origin with an OC/N ratio higher than 20 (e.g., [93]). Since estuaries are environments where both riverine and marine influences are present, the organic matter in surface sediments is composed of both marine and terrestrial sources [55]. In the Krka River estuary, OC/N ratios vary from 4.59 to 8.86, thus indicating dominantly marine, most likely algal or pelagic sources [68].

Based on the sediment analysis results, it can be concluded that sedimentation in the estuary takes place predominantly under the influence of catchment geology, geomorphology, river flow, and biogenic production. A positive correlation was observed between OC and backscatter intensity (r = 0.62) in the mud sediments (Figure 9), and similar observations were made by [9]. The correlations between the OC, magnetic susceptibility, TIC and IR showed various degrees of influence on the backscatter intensities in the fine sediment fractions. This correlation was absent in the coarse carbonate sediments that are a result of the physical disintegration of the submerged tufa barriers.

Although the uncertainty in the estimated accuracy of a classifier depends on the number of samples and the accuracy of the ground truth [94], this study as well as many previous studies [59,95,96] classified results based on a relatively smaller but carefully targeted representative sample number. Overall accuracy assessments show 93.3% in a four-class classification map and 86.7% for a seven-class map, with respective Kappa coefficients of 0.9 for a four-class classification, and 0.83 for a seven-class classification. The use of backscatter data and sediment particle size data, with the addition of MBES data, enabled us to successfully classify the bottom of the study area into four or seven classes. A four-class map is classified into silt, sandy silt, silty sand, and sand, while a seven-class map is classified into fine, medium, coarse, and very coarse silt and fine, medium, and coarse sand. The relationship between sediment particle size and backscatter intensity generally shows that coarser sediment does generate a stronger return, which can be correlated with previous studies [2,6,58,96]. The OBIA-based maps clearly show that coarse-grained sand fraction sediments cover barriers and mounds, while fine-grained sediments cover flatter and deeper areas. The barriers, protruding from the flat bottom, are more susceptible to erosion by the estuarine bottom currents, depriving them of fine-grained sediments and leaving only coarser sediments and plenty of shells and debris (Figure 11). The upstream part of the canyon exhibits somewhat coarser-grained medium silt sediments versus fine silt sediments ranging from Barrier 2 downstream and into Prokljan Lake (Figures 8b and 11h). This can be explained by a more pronounced effect of the Krka River carrying larger particles that are blocked within the canyon by the barriers.

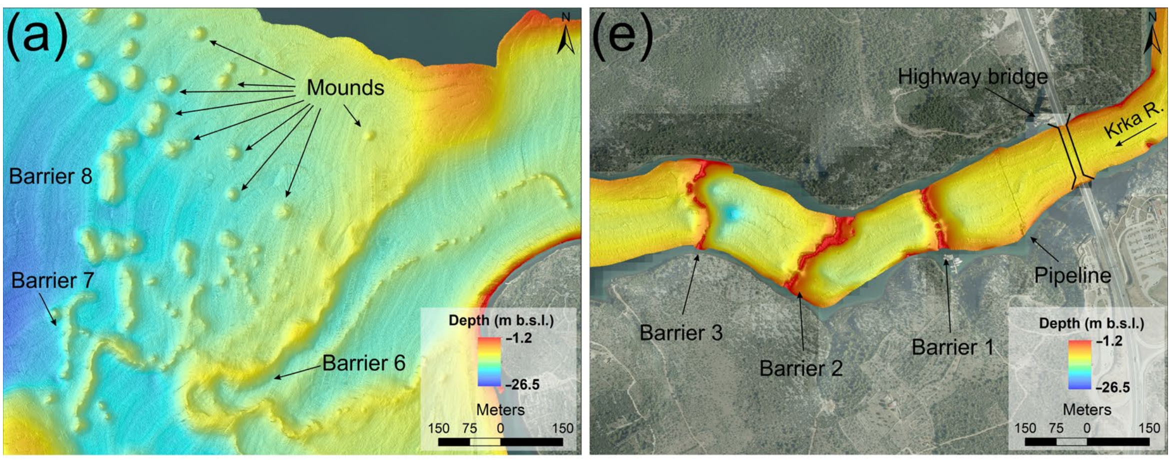

Figure 11. *Cont.*

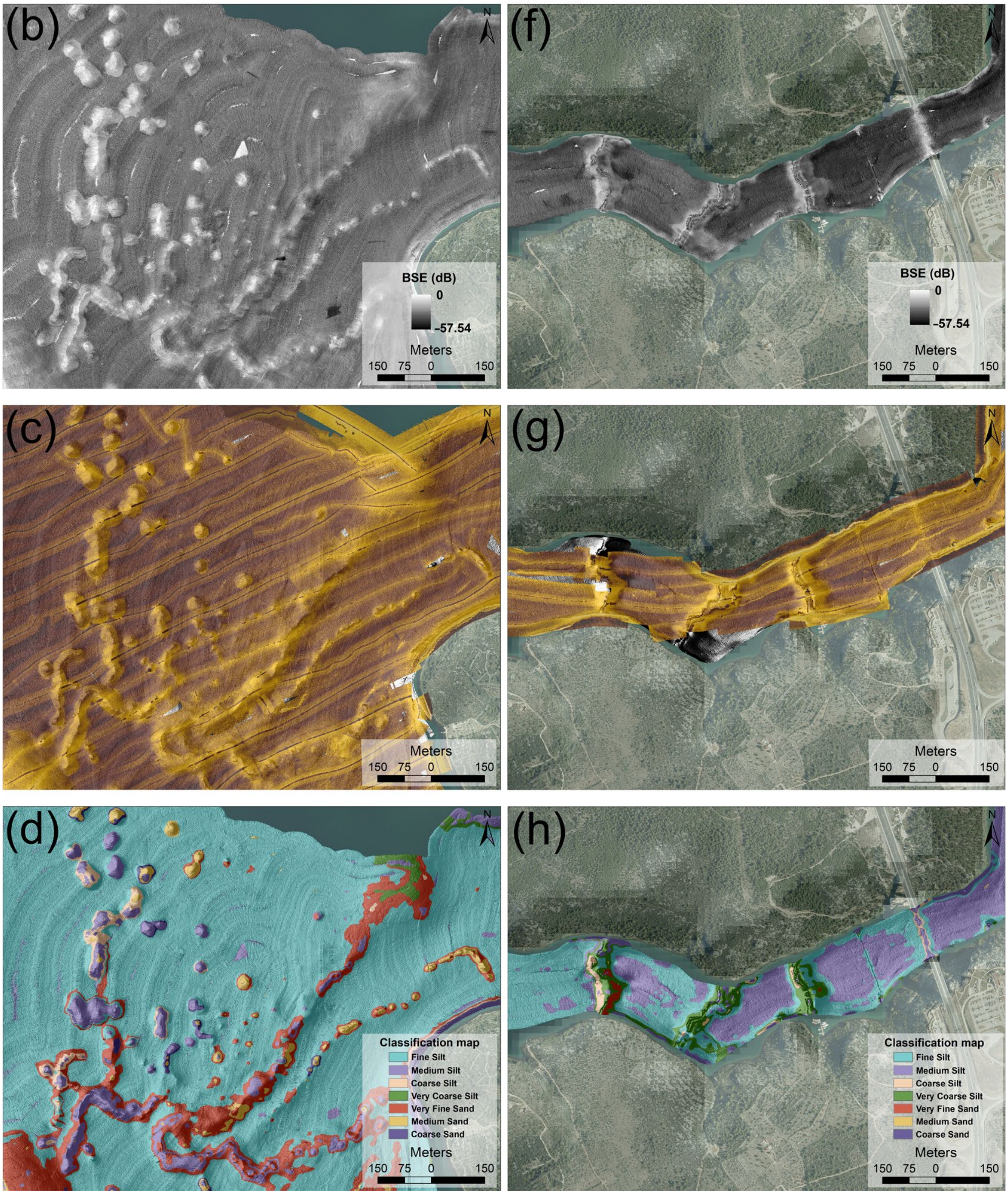

Figure 11. Detailed maps showing submerged barriers and mounds in two parts of the study area (**a**–**d**)—last barriers and mounds at the end of the canyon at the entrance to Prokljan Lake; (**e**–**h**)—barriers at the upstream part in the eastern section of the study area observed with different acoustic methods. (**a**,**e**) MBES map; (**b**,**f**) BSE map; (**c**,**g**) SSS map; (**d**,**h**) a final classification map.

5.2. Origin of Major Geomorphological Features

A classification of the MBES data showed that most of the studied bottom area has a very mild inclination, and less than 1.5% of the area consists of steep slopes or ridges. The most pronounced geomorphological features of the investigated area are well-preserved tufa barriers developed in a submerged Krka River canyon and Prokljan Lake. These unique karst geomorphological features, which grow as algae and mosses encrusted by carbonate, are numerous in the upstream part of the Krka River [17,97]. The investigated barrier system existed before the paleocanyon was flooded. Based on the SBP survey, the thickness of estuarine deposits is approximately 10 m. Four seismic units can be recognized within the study area. Seismic Unit 4 represents a barrier system. Seismic Unit 3 (Figure 6) can be interpreted as lacustrine/fluvial sediments. This unit accumulated before the formation of the estuary with small lakes and waterfalls forming due to barrier growth. The transition between the lower part of Unit 3 and the upper part of Unit 2 is marked by an erosional surface. The scours within Unit 3 developed downstream of the barrier headwalls (Figure 6). The plunge pools initially filled with sediment are scoured, a process that has been well-explained [46–49]. As the pool deepens or the flow velocity is lower, the rate of plunge pool scour decreases forcing them to aggrade [46,50]. Consequently, a higher waterfall and finer grain size create deeper pool depths. Since the tufa barriers continuously grow as long as they are exposed to air, plunge pool scours deepen until the sea level causes a cessation of tufa growth. The scours are similar in shape and depth downstream of Barriers 1, 2, and 3. The scour is somewhat shallower downstream of Barrier 4 and wider downstream of Barrier 5 (Figure 6). This can be explained by the difference in plunge pool size, as well as different barrier shapes and heights [46] (Figure 6d). Barrier 1 also exhibits headwall undercutting, which is a result of lateral and vertical plunge pool erosion [47,48,98,99]. There is no evidence of headwall retreat, which is usually connected to headwall undercutting [48,100], as tufa barriers are "constructive waterfalls", a propagating type of headwall that constantly accumulates and progrades [45]. Sediments of Unit 2 filled and eventually flattened the pool bottom. Unit 2 exhibits a number of weak reflectors. Its transition to Unit 1 is marked by a reflector consisting of a series of hyperbolae. The uniform sediments of Unit 1 without pronounced reflectors can be interpreted as Holocene marine or brackish estuarine sediments deposited until the present. The estuarine sediments first started to accumulate in the deepest part of Prokljan Lake, and the barriers in the middle part of the lake were flooded due to sea ingression. Based on SBP data and the relative sea-level curve [39,101], the riverbed of the paleochannel of the Krka River was at −35 m, the formation of estuarine conditions started at 9500 y BP (Figure 12b), and the sea flooded the last tufa barrier (Barrier B1, at a depth of −4 m, Figure 6) probably some 7500 y BP (Figure 12). Although tufa growth in the Mediterranean region is considered to be restricted to warm periods [31], namely, to stages MIS 1 and MIS 5, [102] argues based on the dating of tufa from the nearby Zrmanja River that the deposition of tufa occurred during the entire MIS 2 and even during MIS 3. Temperatures and CO_2 concentrations rose rapidly during the postglacial period and peaked and stabilized during the Bølling–Allerød period [103], which could have facilitated the growth of the tufa barriers along the course of the Krka River. This would have allowed the barriers to develop for some 5000 to 6000 years before they were flooded by the rising sea levels during the mid-Holocene. As the sea floods the barriers, it prevents further algae and moss growth, as well as CO_2 degassing, causing the cessation of barrier growth. Based on the present-day analog barriers upstream, which have grown for the last 6000–8000 years [31], it can be concluded that during the lower relative sea level with active fluvial processes, the barriers enabled the formation of lakes and waterfalls. Barriers also caused stepwise marine flooding and the formation of the unique estuarine environment in Prokljan Lake between 9000 y BP and 7500 y BP (Figure 12). Thus, the present estuary formed during the late Holocene. According to [97], the conditions for tufa growth in the course of the Krka River have been similar since the early Holocene.

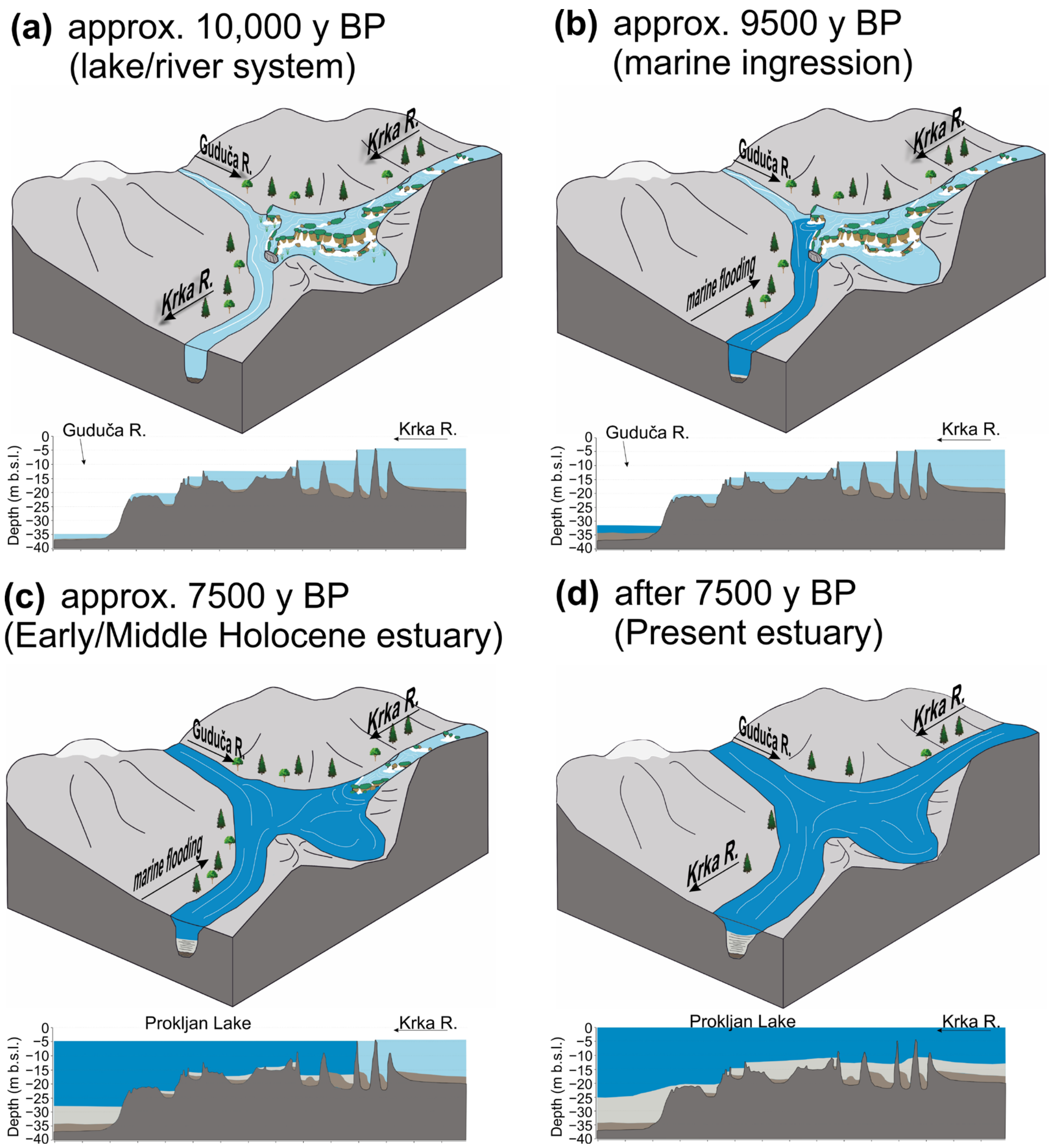

Figure 12. Transformation of the Prokljan Lake area: (**a**) the lowstand environment with a well-developed barrier system; (**b**) the intermediate scenario of marine ingression; (**c**) deeper barriers flooded due to sea-level rise (approximately 9500 y BP until 7500 y BP); (**d**) present state with a formed estuary and completely flooded study area.

6. Conclusions

To utilize the full potential of the MBES/BSE survey, this study integrated several other geophysical surveying methods and seafloor sediment analyses to increase the quality and confidence of the OBIA and geomorphological interpretation of the bottom. Besides the use of PSA analysis of grab samples, a better description of the sediment distribution was achieved with additional inputs, such as videos of the bottom and SSS and SBP analyses. The quality of the geomorphological interpretation of the surveyed bottom was significantly improved by the use of the SBP and SSS survey results, as well as the sediment analyses and videos and images of the bottom. These findings highlight the importance of additional inputs to MBES data to achieve the most accurate results in the definition and segmentation of seafloor classification, geology, and morphology. A four-class classification map achieved an accuracy assessment of 93.3%, while a more complex seven-class map reached 86.7%. A positive correlation between OC and backscatter intensity (r = 0.62) was observed in mud sediments. Correlation was absent in the coarse sediments. The correlations between OC, magnetic susceptibility, IC and IR showed various degrees of influence on the backscatter intensities in the fine sediment fractions. The OC/N ratios varied from 4.59–8.86, thus indicating dominantly marine, most likely algal or pelagic sources. The results of the sediment analysis showed that sedimentation in the estuary takes place predominantly under the influence of catchment geology, geomorphology, river flow, and biogenic production.

This study also created the first geomorphological map of the Krka River estuary and Prokljan Lake, precisely documenting previously unknown or only partially known features. The results of the underwater geomorphology interpretation revealed multiple submerged barriers as the most pronounced geomorphological features. They are analogous to the recent ones that formed upstream in Krka National Park. These submerged barriers formed in the Krka River paleochannel during the late glacial period to the early Holocene, when conditions for their growth were favorable. The SBP survey detected four seismic units within the study area (tufa barriers, lacustrine and fluvial sediments, estuarine sediments). The scours within Unit 3 are evidence of plunge pools created by waterfalls of different shapes and sizes that existed during the sea-level lowstand. The barriers prevented direct marine flooding during the mid-Holocene rapid sea-level rise. Their development seized as the sea level rose during the Holocene sea-level rise and flooded the study area. A successful sediment distribution map based on the MBES and BSE data with additional grab sample grain size analyses revealed a significant difference in the grain size on barriers with larger sand-sized sediments as opposed to flat-bottom parts with finer-grained muddy sediments.

This study shows that further investigations of this dynamic region are necessary, including coring and sediment analyses (comprising geochemical, paleontological and ^{14}C analyses) to better interpret already gathered data and define geomorphological and sedimentary processes under different hydrodynamic conditions from the Holocene to the present.

Supplementary Materials: The following supporting information can be downloaded at: https://www.mdpi.com/article/10.3390/rs15102588/s1, Table S1: Sediment Particle Size; Table S2: Carbon and Nitrogen Analysis; Video S1: Krka_waterfalls_barriers.

Author Contributions: Conceptualization, O.H., N.S., S.M. and D.B.; methodology, O.H.; software, O.H.; validation, N.S., S.M. and D.B.; formal analysis, O.H., N.S., N.I. and M.Š.M.; investigation, O.H., N.S., S.M. and D.B.; resources, S.M. and N.I.; writing—original draft preparation, O.H., S.M. and N.S.; writing—review and editing, D.B. and N.I.; visualization, O.H. and N.S.; project administration, S.M. and N.I.; funding acquisition, S.M. All authors have read and agreed to the published version of the manuscript.

Funding: This work was funded by the Croatian Science Foundation Project "Sediments between source and sink during a late Quaternary eustatic cycle: the Krka River and the Mid Adriatic Deep System" (QMAD) (HRZZ IP-04-2019-8505).

Data Availability Statement: The data presented in this study are available on request from the corresponding author.

Acknowledgments: The authors wish to thank Ivan Razum, Hrvoje Burić, and Marko Copić for their valuable help in the sediment sampling and side-scan surveys. The authors wish to thank all four anonymous reviewers for constructive suggestions and comments that improved our paper.

Conflicts of Interest: The authors declare no conflict of interest. The funders had no role in the design of the study; in the collection, analyses, or interpretation of data; in the writing of the manuscript; or in the decision to publish the results.

References

1. Bellec, V.K.; Bøe, R.; Rise, L.; Lepland, A.; Thorsnes, T.; Bjarnadóttir, L.R. Seabed Sediments (Grain Size) of Nordland VI, Offshore North Norway. *J. Maps* **2017**, *13*, 608–620. [CrossRef]
2. Buhl-Mortensen, L.; Buhl-Mortensen, P.; Dolan, M.F.J.; Holte, B. The MAREANO Programme—A Full Coverage Mapping of the Norwegian off-Shore Benthic Environment and Fauna. *Mar. Biol. Res.* **2015**, *11*, 4–17. [CrossRef]
3. Deiana, G.; Lecca, L.; Melis, R.T.; Soldati, M.; Demurtas, V.; Orrù, P.E. Submarine Geomorphology of the Southwestern Sardinian Continental Shelf (Mediterranean Sea): Insights into the Last Glacial Maximum Sea-Level Changes and Related Environments. *Water* **2021**, *13*, 155. [CrossRef]
4. Erdey-Heydorn, M. An ArcGIS Seabed Characterization Toolbox Developed for Investigating Benthic Habitats. *Mar. Geod.* **2008**, *31*, 318–358. [CrossRef]
5. Deering, R.; Bell, T.; Forbes, D.L.; Campbell, C.; Edinger, E. Morphological Characterization of Submarine Slope Failures in a Semi-Enclosed Fjord, Frobisher Bay, Eastern Canadian Arctic. *Geol. Soc. Lond. Spec. Publ.* **2018**, *477*, 367–376. [CrossRef]
6. Zhi, H.; Siwabessy, J.; Nichol, S.L.; Brooke, B.P. Predictive Mapping of Seabed Substrata Using High-Resolution Multibeam Sonar Data: A Case Study from a Shelf with Complex Geomorphology. *Mar. Geol.* **2014**, *357*, 37–52. [CrossRef]
7. Pillay, T.; Cawthra, H.C.; Lombard, A.T. Characterisation of Seafloor Substrate Using Advanced Processing of Multibeam Bathymetry, Backscatter, and Sidescan Sonar in Table Bay, South Africa. *Mar. Geol.* **2020**, *429*, 106332. [CrossRef]
8. Runya, R.M.; McGonigle, C.; Quinn, R.; Howe, J.; Collier, J.; Fox, C.; Dooley, J.; O'loughlin, R.; Calvert, J.; Scott, L.; et al. Examining the Links between Multi-Frequency Multibeam Backscatter Data and Sediment Grain Size. *Remote Sens.* **2021**, *13*, 1539. [CrossRef]
9. Hunt, C.; Demšar, U.; Dove, D.; Smeaton, C.; Cooper, R.; Austin, W.E.N. Quantifying Marine Sedimentary Carbon: A New Spatial Analysis Approach Using Seafloor Acoustics, Imagery, and Ground-Truthing Data in Scotland. *Front. Mar. Sci.* **2020**, *7*, 588. [CrossRef]
10. Craven, K.F.; McCarron, S.; Monteys, X.; Dove, D. Interaction of Multiple Ice Streams on the Malin Shelf during Deglaciation of the Last British–Irish Ice Sheet. *J. Quat. Sci.* **2021**, *36*, 153–168. [CrossRef]
11. Trottier, A.P.; Lajeunesse, P.; Gagnon-Poiré, A.; Francus, P. Morphological Signatures of Deglaciation and Postglacial Sedimentary Processes in a Deep Fjord-Lake (Grand Lake, Labrador). *Earth Surf. Process. Landf.* **2020**, *45*, 928–947. [CrossRef]
12. Hasan, O.; Miko, S.; Brunović, D.; Papatheodorou, G.; Christodolou, D.; Ilijanić, N.; Geraga, M. Geomorphology of Canyon Outlets in Zrmanja River Estuary and Its Effect on the Holocene Flooding of Semi-Enclosed Basins (The Novigrad and Karin Seas, Eastern Adriatic). *Water* **2020**, *12*, 2807. [CrossRef]
13. Manoutsoglou, E.; Hasiotis, T.; Kyriakoudi, D.; Velegrakis, A.; Lowag, J. Puzzling Micro-Relief (Mounds) of a Soft-Bottomed, Semi-Enclosed Shallow Marine Environment. *Geo-Mar. Lett.* **2018**, *38*, 359–370. [CrossRef]
14. Bendixen, C.; Boldreel, L.O.; Jensen, J.B.; Bennike, O.; Hübscher, C.; Clausen, O.R. Early Holocene Estuary Development of the Hesselø Bay Area, Southern Kattegat, Denmark and Its Implication for Ancylus Lake Drainage. *Geo-Mar. Lett.* **2017**, *37*, 579–591. [CrossRef]
15. Rucińska-Zjadacz, M.; Wróblewski, R. The Complex Geomorphology of a Barrier Spit Prograding into Deep Water, Hel Peninsula, Poland. *Geo-Mar. Lett.* **2018**, *38*, 513–525. [CrossRef]
16. Moreira-Turcq, P.; Martin, J.M.; Fleury, A. Chemical and Biological Characterization of Particles by Flow Cytometry in the Krka Estuary, Croatia. *Mar. Chem.* **1993**, *43*, 115–126. [CrossRef]
17. Korlević, M.; Šupraha, L.; Ljubešić, Z.; Henderiks, J.; Ciglenečki, I.; Dautović, J.; Orlić, S. Bacterial Diversity across a Highly Stratified Ecosystem: A Salt-Wedge Mediterranean Estuary. *Syst. Appl. Microbiol.* **2016**, *39*, 398–408. [CrossRef]
18. Gligora Udovič, M.; Kralj Borojević, K.; Žutinić, P.; Šipoš, L.; Anđelka, P.-M. Net-Phytoplankton Species Dominance in a Travertine Riverine Lake Visovac, NP Krka. *Nat. Croat.* **2011**, *20*, 411–424.
19. Bužančić, M.; Ninčević Gladan, Ž.; Marasović, I.; Kušpilić, G.; Grbec, B.; Matijević, S. Population Structure and Abundance of Phytoplankton in Three Bays on the Eastern Adriatic Coast: Šibenik Bay, Kaštela Bay and Mali Ston Bay. *Acta Adriat.* **2012**, *53*, 413–434.
20. Cetinić, I.; Viličić, D.; Burić, Z.; Olujić, G. Phytoplankton Seasonality in a Highly Stratified Karstic Estuary (Krka, Adriatic Sea). *Hydrobiologia* **2006**, *555*, 31–40. [CrossRef]
21. Fuks, D.; Devescovi, M.; Precali, R.; Krstulović, N.; Šolić, M. Bacterial Abundance and Activity in the Highly Stratified Estuary of the Krka River. *Mar. Chem.* **1991**, *32*, 333–346. [CrossRef]
22. Žutinić, P.; Kulaš, A.; Levkov, Z.; Šušnjara, M.; Orlić, S.; Kukić, S.; Goreta, G.; Valić, D.; Udovič, M.G. Ecological Status Assessment Using Periphytic Diatom Communites—Case Study Krka River. *Maced. J. Ecol. Environ.* **2020**, *22*, 29–44. [CrossRef]
23. Viličić, D.; Legović, T.; Žutić, V. Vertical Distribution of Phytoplankton in a Stratified Estuary. *Aquat. Sci.* **1989**, *51*, 31–46. [CrossRef]
24. Kralj, K.; Plenković-Moraj, A.; Gligora, M.; Primc-Habdija, B.; Šipoš, L. Structure of Periphytic Community on Artificial Substrata: Influence of Depth, Slide Orientation and Colonization Time in Karstic Lake Visovačko, Croatia. *Hydrobiologia* **2006**, *560*, 249–258. [CrossRef]
25. Domínguez-Villar, D.; Cukrov, N.; Krklec, K. Temperature as a Tracer of Hydrological Dynamics in an Anchialine Cave System with a Submarine Spring. *Hydrogeol. J.* **2018**, *26*, 1249–1262. [CrossRef]
26. Legović, T.; Gržetić, Z.; Smirčić, A. Effects of Wind on a Stratified Estuary. *Mar. Chem.* **1991**, *32*, 153–161. [CrossRef]

27. Orlić, M.; Ferenčak, M.; Gržetić, Z.; Limić, N.; Pasarić, Z.; Smirčić, A. High-Frequency Oscillations Observed in the Krka Estuary. *Mar. Chem.* **1991**, *32*, 137–151. [CrossRef]
28. Žutić, V.; Legović, T. A Film of Organic Matter at the Fresh-Water/Sea-Water Interface of an Estuary. *Nature* **1987**, *328*, 612–614. [CrossRef]
29. Cindrić, A.-M.; Garnier, C.; Oursel, B.; Pižeta, I.; Omanović, D. Evidencing the Natural and Anthropogenic Processes Controlling Trace Metals Dynamic in a Highly Stratified Estuary: The Krka River Estuary (Adriatic, Croatia). *Mar. Pollut. Bull.* **2015**, *94*, 199–216. [CrossRef]
30. Cukrov, N.; Barišić, D. Spatial Distribution of 40K And232Th in Recent Sediments of the Krka River Estuary. *Croat. Chem. Acta* **2006**, *79*, 115–118.
31. Horvatinčić, N.; Čalić, R.; Geyh, M.A. Interglacial Growth of Tufa in Croatia. *Quat. Res.* **2000**, *53*, 185–195. [CrossRef]
32. Frančišković-Bilinski, S.; Barišić, D.; Vertačnik, A.; Bilinski, H.; Prohić, E. Characterization of Tufa from the Dinaric Karst of Croatia: Mineralogy, Geochemistry and Discussion of Climate Conditions. *Facies* **2004**, *50*, 183–193. [CrossRef]
33. Lojen, S.; Dolenec, T.; Vokal, B.; Cukrov, N.; Mihelčić, G.; Papesch, W. C and O Stable Isotope Variability in Recent Freshwater Carbonates (River Krka, Croatia). *Sedimentology* **2004**, *51*, 361–375. [CrossRef]
34. Bonacci, O.; Andrić, I.; Roje-Bonacci, T. Hydrological Analysis of Skradinski Buk Tufa Waterfall (Krka River, Dinaric Karst, Croatia). *Environ. Earth Sci.* **2017**, *76*, 669. [CrossRef]
35. Bonacci, O.; Jukić, D.; Ljubenkov, I. Definition of Catchment Area in Karst: Case of the Rivers Krčić and Krka, Croatia. *Hydrol. Sci. J.* **2006**, *51*, 682–699. [CrossRef]
36. Chafetz, H.S.; Srdoc, D.; Horvatincic, N. Early Diagenesis of Plitvice Lakes Waterfall and Barrier Treavertine Deposits. *Géographie Phys. Quat.* **2007**, *48*, 247–255. [CrossRef]
37. Fairbanks, R.G. A 17,000-Year Glacio-Eustatic Sea Level Record: Influence of Glacial Melting Rates on the Younger Dryas Event and Deep-Ocean Circulation. *Nature* **1989**, *342*, 637–642. [CrossRef]
38. Lambeck, K. *Sea Level Change from Mid Holocene to Recent Time: An Australian Example with Global Implications*; American Geophysical Union: Washington, DC, USA, 2011; pp. 33–50. [CrossRef]
39. Vacchi, M.; Marriner, N.; Morhange, C.; Spada, G.; Fontana, A.; Rovere, A. Multiproxy Assessment of Holocene Relative Sea-Level Changes in the Western Mediterranean: Sea-Level Variability and Improvements in the Definition of the Isostatic Signal. *Earth-Sci. Rev.* **2016**, *155*, 172–197. [CrossRef]
40. Juračić, M.; Prohić, E. Mineralogy, Sources of Particles and Sedimentation in the Krka River Estuary (Croatia). *Geološki Vjesn.* **1991**, *44*, 195–200.
41. Burić, Z.; Cetinić, I.; Viličić, D.; Mihalić, K.C.; Carić, M.; Olujić, G. Spatial and Temporal Distribution of Phytoplankton in a Highly Stratified Estuary (Zrmanja, Adriatic Sea). *Mar. Ecol.* **2007**, *28*, 169–177. [CrossRef]
42. Dalrymple, R.W.; Zaitlin, B.A.; Boyd, R. Estuarine Facies Models: Conceptual Basis and Stratigraphic Implications. *J. Sediment. Petrol.* **1992**, *62*, 1130–1146. [CrossRef]
43. Dladla, N.N.; Green, A.N.; Cooper, J.A.G.; Humphries, M.S. Geological Inheritance and Its Role in the Geomorphological and Sedimentological Evolution of Bedrock-Hosted Incised Valleys, Lake St Lucia, South Africa. *Estuar. Coast. Shelf Sci.* **2019**, *222*, 154–167. [CrossRef]
44. De Falco, G.; Carannante, A.; Del Vais, C.; Gasperini, L.; Pascucci, V.; Sanna, I.; Simeone, S.; Conforti, A. Evolution of a Single Incised Valley Related to Inherited Geology, Sea Level Rise and Climate Changes during the Holocene (Tirso River, Sardinia, Western Mediterranean Sea). *Mar. Geol.* **2022**, *451*, 106885. [CrossRef]
45. Goudie, A.S. Waterfalls: Forms, Distribution, Processes and Rates of Recession. *Quaest. Geogr.* **2020**, *39*, 59–77. [CrossRef]
46. Scheingross, J.S.; Lamb, M.P. Sediment Transport through Self-adjusting, Bedrock-walled Waterfall Plunge Pools. *J. Geophys. Res. Earth Surf.* **2016**, *121*, 939–963. [CrossRef]
47. Scheingross, J.S.; Lo, D.Y.; Lamb, M.P. Self-formed Waterfall Plunge Pools in Homogeneous Rock. *Geophys. Res. Lett.* **2017**, *44*, 200–208. [CrossRef]
48. Lamb, M.P.; Howard, A.D.; Dietrich, W.E.; Perron, J.T. Formation of Amphitheater-Headed Valleys by Waterfall Erosion after Large-Scale Slumping on Hawai'i. *Geol. Soc. Am. Bull.* **2007**, *119*, 805–822. [CrossRef]
49. Gordon, N.D.; McMahon, T.A.; Finlayson, B.L.; Gippel, C.J.; Nathan, R.J. *Stream Hydrology: An Introduction for Ecologists*, 2nd ed.; John Wiley and Sons: Chichester, UK, 2004; ISBN 0470843578.
50. Babazadeh, H.; Ashourian, M.; Shafai-Bajestan, M. Experimental Study of Headcut Erosion in Cohesive Soils under Different Consolidation Types and Hydraulic Parameters. *Environ. Earth Sci.* **2017**, *76*, 438. [CrossRef]
51. Haviv, I.; Enzel, Y.; Whipple, K.X.; Zilberman, E.; Matmon, A.; Stone, J.; Fifield, K.L. Evolution of Vertical Knickpoints (Waterfalls) with Resistant Caprock: Insights from Numerical Modeling. *J. Geophys. Res.* **2010**, *115*, F03028. [CrossRef]
52. Diesing, M.; Kröger, S.; Parker, R.; Jenkins, C.; Mason, C.; Weston, K. Predicting the Standing Stock of Organic Carbon in Surface Sediments of the North–West European Continental Shelf. *Biogeochemistry* **2017**, *135*, 183–200. [CrossRef]
53. Kemp, A.L.W. Organic Carbon and Nitrogen in the Surface Sediments of Lakes Ontario, Erie and Huron. *J. Sediment. Petrol.* **1971**, *41*, 537–548.
54. Meyers, P.A. Preservation of Elemental and Isotopic Source Identification of Sedimentary Organic Matter. *Chem. Geol.* **1994**, *114*, 289–302. [CrossRef]

55. Gao, X.; Yang, Y.; Wang, C. Geochemistry of Organic Carbon and Nitrogen in Surface Sediments of Coastal Bohai Bay Inferred from Their Ratios and Stable Isotopic Signatures. *Mar. Pollut. Bull.* **2012**, *64*, 1148–1155. [CrossRef]
56. Gu, Y.-G.; Ouyang, J.; Ning, J.-J.; Wang, Z.-H. Distribution and Sources of Organic Carbon, Nitrogen and Their Isotopes in Surface Sediments from the Largest Mariculture Zone of the Eastern Guangdong Coast, South China. *Mar. Pollut. Bull.* **2017**, *120*, 286–291. [CrossRef]
57. Stephens, D.; Diesing, M. A Comparison of Supervised Classification Methods for the Prediction of Substrate Type Using Multibeam Acoustic and Legacy Grain-Size Data. *PLoS ONE* **2014**, *9*, e93950. [CrossRef]
58. Montereale Gavazzi, G.; Madricardo, F.; Janowski, L.; Kruss, A.; Blondel, P.; Sigovini, M.; Foglini, F. Evaluation of Seabed Mapping Methods for Fine-Scale Classification of Extremely Shallow Benthic Habitats—Application to the Venice Lagoon, Italy. *Estuar. Coast. Shelf Sci.* **2016**, *170*, 45–60. [CrossRef]
59. Janowski, Ł.; Tęgowski, J.; Nowak, J. Seafloor Mapping Based on Multibeam Echosounder Bathymetry and Backscatter Data Using Object-Based Image Analysis: A Case Study from the Rewal Site, the Southern Baltic. *Oceanol. Hydrobiol. Stud.* **2018**, *47*, 248–259. [CrossRef]
60. Innangi, S.; Tonielli, R.; Romagnoli, C.; Budillon, F.; Di Martino, G.; Innangi, M.; Laterza, R.; Le Bas, T.; Lo Iacono, C. Seabed Mapping in the Pelagie Islands Marine Protected Area (Sicily Channel, Southern Mediterranean) Using Remote Sensing Object Based Image Analysis (RSOBIA). *Mar. Geophys. Res.* **2019**, *40*, 333–355. [CrossRef]
61. Biondo, M.; Bartholomä, A. A Multivariate Analytical Method to Characterize Sediment Attributes from High-Frequency Acoustic Backscatter and Ground-Truthing Data (Jade Bay, German North Sea Coast). *Cont. Shelf Res.* **2017**, *138*, 65–80. [CrossRef]
62. Vlahović, I.; Tišljar, J.; Velić, I.; Matičec, D. Evolution of the Adriatic Carbonate Platform: Palaeogeography, Main Events and Depositional Dynamics. *Palaeogeogr. Palaeoclimatol. Palaeoecol.* **2005**, *220*, 333–360. [CrossRef]
63. Mamužić, P. *Tumač Za Osnovnu Geološku Kartu 1: 100 000 List Šibenik K 33-8 (Basic geological map of the Republic of Croatia 1: 100 00. Explanatory notes for sheet Mohač)*; Institut za Geološka Istražicanja: Zagreb, Croatia, 1975; p. 37.
64. Liu, J.; Hrustić, E.; Du, J.; Gašparović, B.; Čanković, M.; Cukrov, N.; Zhu, Z.; Zhang, R. Net Submarine Groundwater-Derived Dissolved Inorganic Nutrients and Carbon Input to the Oligotrophic Stratified Karstic Estuary of the Krka River (Adriatic Sea, Croatia). *J. Geophys. Res. Ocean.* **2019**, *124*, 4334–4349. [CrossRef]
65. Legović, T.; Žutić, V.; Gržetić, Z.; Cauwet, G.; Precali, R.; Viličić, D. Eutrophication in the Krka Estuary. *Mar. Chem.* **1994**, *46*, 203–215. [CrossRef]
66. Buljan, M. Neka Hidrografska Svojstva Estuarnih Područja Rijeka Krke i Zrmanje. *Krš Jugoslavije* **1969**, *20*, 303–326.
67. Prohić, E.; Juračić, M. Heavy Metals in Sediments-Problems Concerning Determination of the Anthropogenic Influence. Study in the Krka River Estuary, Eastern Adriatic Coast, Yugoslavia. *Environ. Geol. Water Sci.* **1989**, *13*, 145–151. [CrossRef]
68. Svensen, C.; Viličić, D.; Wassmann, P.; Arashkevich, E.; Ratkova, T. Plankton Distribution and Vertical Flux of Biogenic Matter during High Summer Stratification in the Krka Estuary (Eastern Adriatic). *Estuar. Coast. Shelf Sci.* **2007**, *71*, 381–390. [CrossRef]
69. Cukrov, N.; Barišić, D.; Juračić, M. Calculated Sedimentation Rate in the Krka River Estruary Using Vertical Diostribution of 137Cs. In *38th CIESM Congress Proceedings*; Frédéric, B., Dimitris, S., Jordi, F., Nicholas, F., Eds.; CIESM: Istanbul, Turkey, 2007; p. 81.
70. Cukrov, N.; Doumandji, N.; Garnier, C.; Tucaković, I.; Dang, D.H.; Omanović, D.; Cukrov, N. Anthropogenic Mercury Contamination in Sediments of Krka River Estuary (Croatia). *Environ. Sci. Pollut. Res.* **2020**, *27*, 7628–7638. [CrossRef]
71. Winton, T. Quantifying Depth of Burial and Composition of Shallow Buried Archaeological Material: Integrated Sub-Bottom Profiling and 3D Survey Approaches. In *3D Recording and Interpretation for Maritime Archaeology*; Springer: Cham, Switzerland, 2019; Volume 37, pp. 155–174.
72. Wunderlich, J.; Müller, S. High-Resolution Sub-Bottom Profiling Using Parametric Acoustics. *Int. Ocean Syst.* **2003**, *7*, 6–11.
73. Wang, F.; Dong, L.; Ding, J.; Zhou, X.; Tao, C.; Lin, X.; Liang, G. An Experiment of the Actual Vertical Resolution of the Sub-Bottom Profiler in an Anechoic Tank. *Arch. Acoust.* **2019**, *44*, 185–194. [CrossRef]
74. Horn, B.K.P. Hill Shading and the Reflectance Map. *Proc. IEEE* **1981**, *69*, 14–47. [CrossRef]
75. Dolan, M.F.J. Calculation of Slope Angle from Bathymetry Data Using GIS—Effects of Computation Algorithm, Data Resolution and Analysis Scale. In *Geology for Society*; Geological Survey of Norway: Trondheim, Norway, 2012; p. 44.
76. Zevenbergen, L.W.; Thorne, C.R. Quantitative Analysis of Land Surface Topography. *Earth Surf. Process. Landf.* **1987**, *12*, 47–56. [CrossRef]
77. Minár, J.; Evans, I.S.; Jenčo, M. A Comprehensive System of Definitions of Land Surface (Topographic) Curvatures, with Implications for Their Application in Geoscience Modelling and Prediction. *Earth-Sci. Rev.* **2020**, *211*, 103414. [CrossRef]
78. Walbridge, S.; Slocum, N.; Pobuda, M.; Wright, D.J. Unified Geomorphological Analysis Workflows with Benthic Terrain Modeler. *Geosciences* **2018**, *8*, 94. [CrossRef]
79. Allen, J.R.L.; Thornley, D.M. Laser Granulometry of Holocene Estuarine Silts: Effects of Hydrogen Peroxide Treatment. *Holocene* **2004**, *14*, 290–295. [CrossRef]
80. Blott, S.J.; Pye, K. Gradistat: A Grain Size Distribution and Statistics Package for the Analysis of Unconsolidated Sediments. *Earth Surf. Process. Landforms* **2001**, *26*, 1237–1248. [CrossRef]
81. Folk, R.L.; Ward, W.C. Brazos River Bar: A Study in the Significance of Grain Size Parameter. *J. Sediment. Petrol.* **1957**, *27*, 3–26. [CrossRef]

82. Diesing, M.; Green, S.L.; Stephens, D.; Lark, R.M.; Stewart, H.A.; Dove, D. Mapping Seabed Sediments: Comparison of Manual, Geostatistical, Object-Based Image Analysis and Machine Learning Approaches. *Cont. Shelf Res.* **2014**, *84*, 107–119. [CrossRef]
83. Hasan, R.C.; Ierodiaconou, D.; Laurenson, L.; Schimel, A. Integrating Multibeam Backscatter Angular Response, Mosaic and Bathymetry Data for Benthic Habitat Mapping. *PLoS ONE* **2014**, *9*, e97339. [CrossRef]
84. Demirović, D. An Implementation of the Mean Shift Algorithm. *Image Process. Line* **2019**, *9*, 251–268. [CrossRef]
85. Breiman, L. Random Forests. *Mach. Learn.* **2001**, *45*, 5–32. [CrossRef]
86. Bosch, A.; Zisserman, A.; Munoz, X. Image Classification Using Random Forests and Ferns. In Proceedings of the 2007 IEEE 11th International Conference on Computer Vision, Rio de Janeiro, Brazil, 14–21 October 2007; pp. 1–8.
87. Dearing, J.A.; Dann, R.J.L.; Hay, K.; Lees, J.A.; Loveland, P.J.; Maher, B.A.; O'Grady, K. Frequency-Dependent Susceptibility Measurements of Environmental Materials. *Geophys. J. Int.* **1996**, *124*, 228–240. [CrossRef]
88. Mayer, L.M. Surface Area Control of Organic Carbon Accumulation in Continental Shelf Sediments. *Geochim. Cosmochim. Acta* **1994**, *58*, 1271–1284. [CrossRef]
89. Tyson, R.V. *Sedimentary Organic Matter*; Springer: Dordrecht, The Netherlands, 1995; ISBN 978-94-010-4318-2.
90. Cowie, G.L.; Hedges, J.I. Organic Carbon and Nitrogen Geochemistry of Black Sea Surface Sediments from Stations Spanning the Oxic:Anoxic Boundary. In *Black Sea Oceanography*; Izdar, E., Murray, J.W., Eds.; Kluwer Academic Publishers: Norwell, MA, USA, 1991; pp. 343–359.
91. Faust, J.C.; Knies, J. Organic Matter Sources in North Atlantic Fjord Sediments. *Geochem. Geophys. Geosyst.* **2019**, *20*, 2872–2885. [CrossRef]
92. Lamb, A.L.; Wilson, G.P.; Leng, M.J. A Review of Coastal Palaeoclimate and Relative Sea-Level Reconstructions Using Δ13C and C/N Ratios in Organic Material. *Earth-Sci. Rev.* **2006**, *75*, 29–57. [CrossRef]
93. Saito, Y.; Nishimura, A.; Matsumoto, E. Transgressive Sand Sheet Covering the Shelf and Upper Slope off Sendai, Northeast Japan. *Mar. Geol.* **1989**, *89*, 245–258. [CrossRef]
94. Carlotto, M.J. Effect of Errors in Ground Truth on Classification Accuracy. *Int. J. Remote Sens.* **2009**, *30*, 4831–4849. [CrossRef]
95. Micallef, A.; Foglini, F.; Le Bas, T.; Angeletti, L.; Maselli, V.; Pasuto, A.; Taviani, M. The Submerged Paleolandscape of the Maltese Islands: Morphology, Evolution and Relation to Quaternary Environmental Change. *Mar. Geol.* **2013**, *335*, 129–147. [CrossRef]
96. Brown, C.J.; Beaudoin, J.; Brissette, M.; Gazzola, V. Multispectral Multibeam Echo Sounder Backscatter as a Tool for Improved Seafloor Characterization. *Geosciences* **2019**, *9*, 126. [CrossRef]
97. Lojen, S.; Cukrov, N.; Papesch, W.; Mihelčić, G. Precipitation of Tufa Barriers from Krka River, Croatia. In Proceedings of the International Symposium on Isotope Hydrology and Integrated Water Resources Management. Book of Extended Synopses, Vienna, Austria, 19–23 May 2003; p. 366.
98. Scheingross, J.S.; Lamb, M.P.; Fuller, B.M. Self-Formed Bedrock Waterfalls. *Nature* **2019**, *567*, 229–233. [CrossRef]
99. Alexandrowicz, Z. Geologically Controlled Waterfall Types in the Outer Carpathians. *Geomorphology* **1994**, *9*, 155–165. [CrossRef]
100. Hayakawa, Y.S.; Yokoyama, S.; Matsukura, Y. Erosion Rates of Waterfalls in Post-Volcanic Fluvial Systems around Aso Volcano, Southwestern Japan. *Earth Surf. Process. Landf.* **2008**, *33*, 801–812. [CrossRef]
101. Lambeck, K.; Antonioli, F.; Anzidei, M.; Ferranti, L.; Leoni, G.; Scicchitano, G.; Silenzi, S. Sea Level Change along the Italian Coast during the Holocene and Projections for the Future. *Quat. Int.* **2011**, *232*, 250–257. [CrossRef]
102. Barešić, J.; Faivre, S.; Sironić, A.; Borković, D.; Lovrenčić Mikelić, I.; Drysdale, R.N.; Krajcar Bronić, I. The Potential of Tufa as a Tool for Paleoenvironmental Research—A Study of Tufa from the Zrmanja River Canyon, Croatia. *Geosciences* **2021**, *11*, 376. [CrossRef]
103. Clark, P.U.; Shakun, J.D.; Baker, P.A.; Bartlein, P.J.; Brewer, S.; Brook, E.; Carlson, A.E.; Cheng, H.; Kaufman, D.S.; Liu, Z.; et al. Global Climate Evolution during the Last Deglaciation. *Proc. Natl. Acad. Sci. USA* **2012**, *109*, E1134–E1142. [CrossRef]